Applied Energy 406 (2026) 127275

Contents lists available at ScienceDirect

Applied Energy

journal homepage: www.elsevier.com/locate/apenergy

Assessment of offshore power potential in Zhoushan archipelago using a 45-year wind field product

Honghuan Zhi [a], Han Liu [b], Liqin Zhou [b], Yifan Zhou [a], Feixiang Li [a], Xiaoran Wei [a], Yefei Bai [a,c,*]

[a] Ocean College, Zhejiang University, Zhoushan 316021, China
[b] Zhoushan Meteorology Bureau, Zhoushan 316000, China
[c] Hainan Institute, Zhejiang University, Sanya, Hainan 572025, China

HIGHLIGHTS

- Offshore wind energy in Zhoushan Archipelago is assessed using 45-year wind product.
- Islands-Oriented Multi-Factor Assessment is proposed for resource classification.
- Potential wind farm locations are identified through GIS-based spatial planning.

GRAPHICAL ABSTRACT

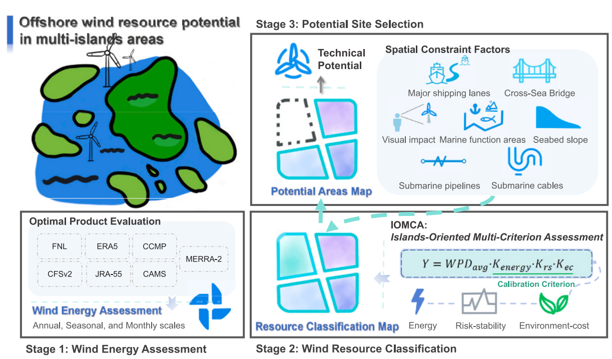

ARTICLE INFO

Keywords:
Wind energy
Multi-criterion assessment
Resource classification
Spatial planning
Zhoushan archipelago

ABSTRACT

The growing demand for sustainable offshore wind energy has heightened the need for accurate wind resource assessment and feasible turbine deployment. Conventional multi-factor assessments fall short of identifying wind energy hotspots in multiple islands environment. This study proposes a three-stage wind resource assessment framework aimed to capture inter-island variations of wind resources across Zhoushan Archipelago. A long-term wind energy assessment at 100 m height is first conducted by using the optimal product through inter-comparison of seven mainstream global wind datasets against observations from ten evenly distributed sites. An Islands-Oriented Multi-Criterion assessment method, integrating energy, risk-stability, and environmental-cost factors, is then proposed to classify wind resources. Unconstrained offshore wind turbine zones are identified in the end through GIS-based spatial planning. Zhoushan Archipelago demonstrates substantial wind energy potential, with most areas exhibiting annual wind power density of about 420–550 W/m^2 but notable spatiotemporal variability, particularly low stability in central regions. The maximum energy potential concentrates in southeastern open seas (500–550 W/m^2), with values gradually decreasing westward and exhibiting moderate levels near Hangzhou Bay (360–440 W/m^2). The optimal turbine deployment zones are identified around Yushan Island, followed by Hangzhou Bay and east of Shanghai. Unconstrained suitable areas yield maximum technical potential of 29.48 TWh/yr. These findings provide actionable insights for wind energy

* Corresponding author at: Ocean College, Zhejiang University, Zhoushan 316021, China.
E-mail address: yfbai@zju.edu.cn (Y. Bai).

https://doi.org/10.1016/j.apenergy.2025.127275
Received 4 June 2025; Received in revised form 25 November 2025; Accepted 13 December 2025
Available online 17 December 2025

planning in Zhoushan and other multi-island regions globally, emphasizing spatial prioritization and resource optimization.

1. Introduction

Global carbon dioxide emissions have been rapidly increasing since the 21st century and hit a historic high in 2021 [1]. Following the same trend, the global temperature is projected to exceed 2.8 °C by the end of this century [2]. With the boosting requirements of energy transition for sustainable social and economic development, renewable energy has emerged as a long-term solution for achieving decarbonization [3,4]. Wind energy stands out from a list of renewable resources with charming attributes of high performance, cost-effectiveness, safety, and eco-friendliness [5,6]. The development of the offshore wind energy, in particular, has shown a steady upward trajectory by accounting for an average of 25 % of new global offshore installations from 2020 to 2024 [7–9]. The global installed offshore wind power capacity reached 83.2 GW in 2024, with 8.0 GW added in that year alone. And the capacity is expected to surpass 239 GW by 2030. The offshore wind energy sector in China has also undergone rapid expansion, with capacity reaching nearly 45 GW by late 2024, representing 54 % of the global offshore wind installations [7]. By virtue of strong offshore wind and extensive shallow-water regions, Zhoushan, an archipelago city in Zhejiang Province adjacent to Shanghai, has become one of the leading cities for offshore wind energy industries in China [10,11]. Nearly 1 GW of offshore wind capacity had been completed construction in Zhoushan by the end of 2024, with an additional 1.77 GW under construction, forming it the largest offshore wind cluster of Zhejiang Province [12]. The number of cumulative offshore wind turbines is even expected to increase further in Zhoushan. However, in-depth investigations of wind energy potential for regions with competitive wind resource endowment across China seas are still incomplete, particularly for multi-island regions [13]. Therefore, in Zhejiang, fast-growing offshore wind industry substantially requires trustworthy wind resource assessments over Zhoushan Archipelago to guide imminent future development.

Traditional assessments primarily rely on wind field records taken from fixed meteorological towers, anchored buoys, vessels, and ships [14]. However, the high investment and maintenance cost and the limited spatiotemporal coverage significantly hamper the construction of high-resolution resource maps for evaluation [15]. Regional weather prediction models, such as the Weather Research and Forecasting model [16], the Consortium for Small-Scale Modeling [17], and Regional Atmospheric Modeling System [18], are capable of accurately describing long-term wind field evolution in refined spatial resolutions [19]. Achieving optimal performance, however, requires advanced modeling skills to minimize sensitivity to computational domains, optimize physical parameters, and speed-up data assimilation, as well as higher computational costs [20,21]. Recent advances in machine learning techniques show considerable potential for wind fields reconstruction and prediction [22,23]. However, their reliability depends not only on high computational resources and well-designed model architectures, but also on large volumes of high-quality datasets for training and validation [24,25]. In recent years, the rapid development of multi-source environmental observation systems, such as satellite remote sensing, marine-atmosphere coupled monitoring networks, and offshore measurement platforms, together with the development of modern weather forecasting models, has substantially improved the data availability for generating widely accessible global wind field products [26–28]. These products are broadly accepted as a cost-effective toolbox for wind energy industries to conduct energy assessments at global and regional scales [29–33] owing to their merits of high grid resolution, fewer data gaps, wide-ranging spatiotemporal coverage, and multiple atmospheric and oceanic variables [34]. The global wind datasets can be generally divided into three categories: analyses represented by the Final Global Tropospheric Analysis (FNL) and Global Forecast System; reanalysis such as the fifth-generation of the ECMWF reanalysis (ERA5), Climate Forecast System Reanalysis version 2 (CFSv2), second Modern-Era Retrospective analysis for Research and Applications (MERRA-2), Japanese 55-year Reanalysis (JRA-55), and the Copernicus Atmosphere Monitoring Service (CAMS); multi-source synthetic products, for example, Cross-Calibrated Multi-Platform (CCMP). Owing to existing differences in the applied forecast models, observational data, and assimilation schemes, the performance of these products in reproducing accurate wind evolution varies considerably from place to place [35]. Therefore, it is of great importance to first identify the most reliable one for the designated wind potential area before the assessment takes place.

Evaluation studies on wind products have been carried out widely in different regions. Carvalho et al. [36] analyzed the performance of CCMP and several QuickSCAT-derived products over the Iberian Peninsula region through comparison with five buoy measurements and found that CCMP has high accuracy in describing local wind regime characteristics. Alvarez et al. [37] compared six surface wind datasets (CCMP, CFSR, NCEP-R2, ERA-Interim, MERRA, and QuickSCAT) against wind records of four ocean buoys in the southern Bay of Biscay from 2000 to 2009, and their error analysis indicates CCMP performs slightly better with the lowest bias and RMSE. Carvalho [38] assessed the quality of MERRA-2 as well as CFSR, ERA-Interim, JRA-55, MERRA by comparing them with 10 years of measurements from a wide range of surface wind observing platforms. Statistical analysis shows that MERRA-2 presents a clear improvement over its predecessor and is able to provide comparable estimations with other products in terms of representing the global near-surface wind fields. Miao et al. [39] assessed near-surface wind speeds from four reanalysis datasets (ERA-Interim, JRA-55, CFS, and MERRA-2) by comparing them to monthly-averaged observations from 1038 inland stations (1980–2016). The results suggest that JRA-55 and CFS offer the best estimates of annual and seasonal variabilities in the Northern Hemisphere. Wang et al. [40] compared monthly-averaged surface wind speeds of four reanalysis (CCMP, ERA-Interim, JRA-55, CFSR) with observations recorded at ten nearshore sites (1988–2015) in China, and the statistical indices show JRA-55 maintains the lowest bias and RMSE in reproducing long-term wind speeds at offshore area. Nowadays, the unceasingly emerging and progressively updated wind-field data products present noticeable improvements over their predecessors [32,41–43] and provide more options for reproducing wind speed and direction. Nevertheless, owing to the local dependency of wind characteristics, the optimal product for many wind-rich regions remains uncertain. A number of evenly distributed observation stations across the interest regions constitute a critical arrangement to guarantee the validity of product inter-comparison in the first place and proceed to the energy assessment next.

The wind energy assessment has been evolving rapidly. Earlier studies mainly focused on climatic assessment, which provides global or regional quantitative characterization of offshore wind power density (WPD) [44–47]. More recently, the approach shifts to multi-factor assessment, integrating various localized control factors to assist wind energy development. Based on the Delphi method of decision-making, Zheng et al. [48,49] proposed a classification scheme by considering factors associated with wind energy, environmental risk, and cost to calculate expectations for offshore site selection. While the implemented weighted-additive method balances diverse factors, the linear summation formulation of the method can be difficult to describe high-gradient distributions of the resultant expectations, particularly in complex environment. Moreover, the assignment of factor weights in the formulation is typically based on experts' judgments, which may inevitably introduce subjectivity and sensitivity in identification of optimal sites [50]. Abramic et al. [51] introduced an analytic hierarchy process (AHP)-based decision support system in the Canary Islands to analyze relationships between the offshore wind energy facilities and five cluster parameters regarding oceanographic potential, environmental sensibility, restrictions of marine conservation, land-sea interactions, and potential conflict with maritime activities respectively. Suitability maps are developed from the system to identify marine areas that have significant wind potential but minimal impact on the marine environment. The results, however, are sensitive to experts' pairwise comparisons, which can vary subjectively depending on individual backgrounds and preferences [52]. In assessing offshore wind power potential of the exclusive economic zone of Pakistan, Tahir et al. [53] applied a sequential elimination approach by excluding areas that fail to meet thresholds for wind velocity, water depth, and distance from shore, together with spatial restrictions of international shipping routes and underwater internet cabling, in order to select suitable offshore wind farm sites for performance and environmental impact study. This assessment offers a straightforward way to conduct preliminary site screening, whereas the reliance on limited wind energy factors and strict thresholds falls short of capturing detailed regional variations and may overlook potentially suitable locations [54]. To assess offshore wind resources along the Indian coast, Patel et al. [55] utilized the ERA5 wind products and presented the Optimal Hotspot Identifier (OHI) method to rapidly locate and characterize offshore wind farm sites. The index combines with wind resource availability, monthly variability, and frequency of exploitable wind energy can serve as a simple support tool to help decision-makers achieve various policy targets. Although this method supports macroscopic analysis, the limited influential factors and the difficulty of proper weight-balance between unnormalized factors constraints its ability to reveal localized patterns in multi-criteria decision support.

Effective offshore wind energy planning in multi-island regions with complex environmental conditions demands a method capable of capturing regional variations and highlighting optimal development sites. To this end, we propose a three-stage methodological framework encompassing wind energy assessment, wind resource classification, and site selection. The Zhoushan Archipelago, characterized by complex multi-island geography, competitive offshore wind energy resources, and extensive ongoing offshore wind energy development, is used here as a representative case study. In particular, a new resource classification methodology, namely Islands-Oriented Multi-Criterion Assessment (IOMCA), is developed to capture detailed regional resource variations across the study area and identify potential offshore wind turbine sites. The remainder of this paper is organized as follows. Section 2 describes the study area and observational datasets, followed by a detailed explanation of methods in Section 3. Section 4 presents the results corresponding to the three stages of the methodology framework, and Section 5 discusses the contributions and implications of this study for offshore wind development. The conclusions and prospects are summarized in Section 6.

2. Study area and observational data

Zhoushan is the first prefecture-level island city in the eastern

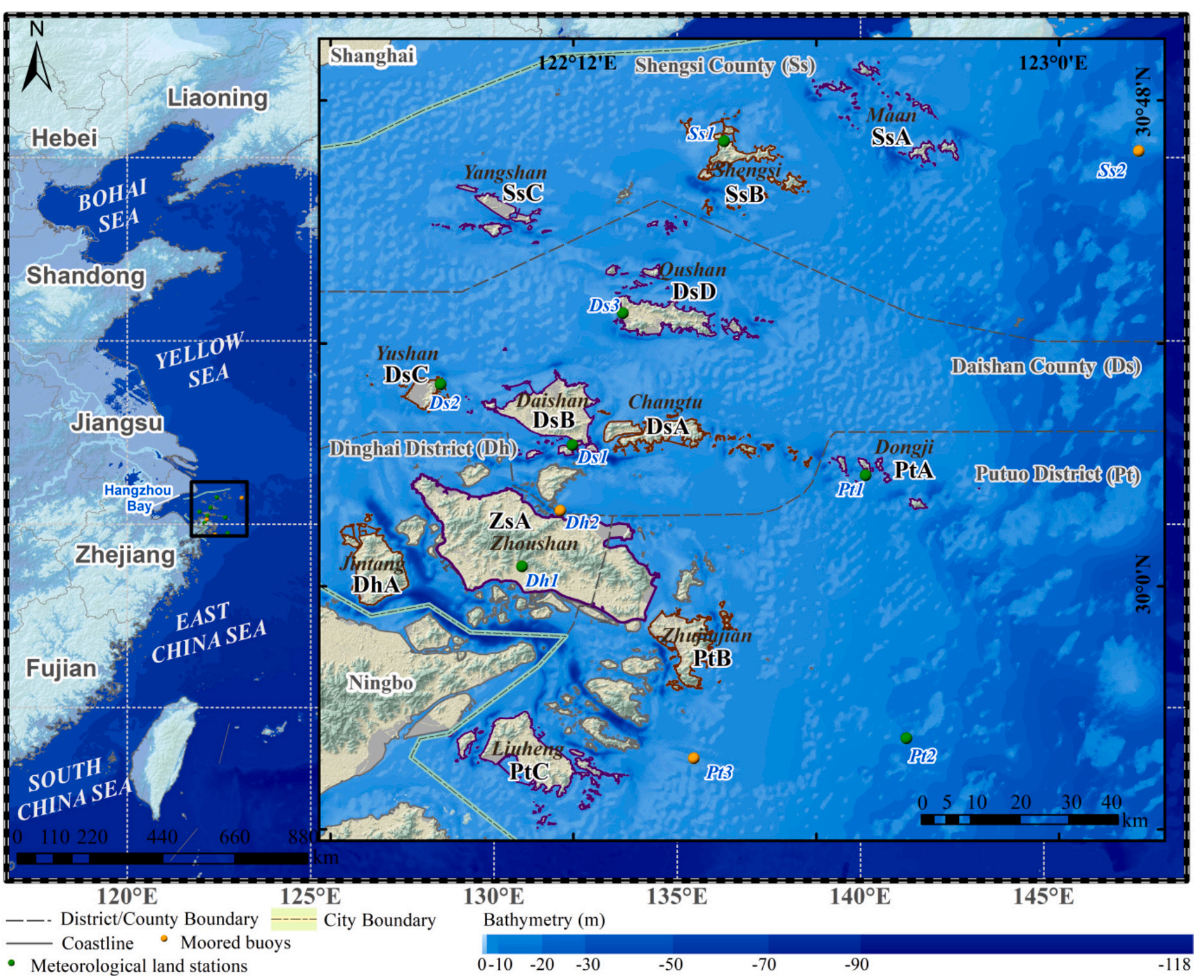

Fig. 1. Location and map of Zhoushan Archipelago. Adjacent island groups are distinguished by purple-red contrasting shoreline colors. (For interpretation of the references to colour in this figure legend, the reader is referred to the web version of this article.)

Chinese province of Zhejiang. It is located at the exterior margin of trumpet-shaped Hangzhou Bay and close to Ningbo City in the south and Shanghai City in the north (Fig. 1). It consists of China's largest archipelago of 2085 islands distributed across two districts, Dinghai (Dh) and Putuo (Pt), and two counties, Daishan (Ds) and Shengsi (Ss) [56]. It covers a total area of 22,000 km^2, including a sea area of about 20,800 km^2. The six major islands with over 50 km^2 land area are Zhoushan Island (ZsA, 503 km^2), Daishan Island (DsB, 119 km^2), Liuheng Island (PtC, 109 km^2), Jintang Island (DhA, 82 km^2), Zhujiajian Island (PtB, 76 km^2), and Qushan Island (DsD, 74 km^2). In addition, numerous smaller island groups scattered across the Zhoushan, such as Changtu Islands (DsA, 54 km^2), Shengsi Islands (SsB, 38.33 km^2), Yangshan Islands (SsC, 23 km^2), Yushan Islands (DsC, 21 km^2), Maan Islands (SsA, 20 km^2), and Dongji Islands (PtA, 12 km^2), contribute to a highly fragmented and discontinuous coastline with a total length of approximately 2788 km, compared with the estimated 300 km for Hangzhou Bay.

Ten observational sites with relatively even distribution over the study area are selected to come up with hourly wind records from 00:00 on Jan. 1st to 23:00 on Dec. 31st in 2018 for comparison. Seven of them, including Dh1, Ds1, Ds2, Ds3, Pt1, Pt2, and Ss1, are meteorological land stations marked as green points in Fig. 1. Three of them, which are composed of Dh2, Pt3, and Ss2, are moored buoys marked as orange points in Fig. 1. The wind data measured by moored buoys are vertically interpolated within the atmospheric boundary layer to the 10 m standard height through implementation of the logarithmic wind profile [57] in order to be consistent with those from meteorological land stations. For clarity, all islands and observational sites in this paper follow a three-character abbreviation scheme, where the first two letters indicate the administrative region and the last letter/number specifies the island (A, B, C, D) or the station (1,2,3), except for Island ZsA, which spans both Dh and Pt districts and is denoted independently of administrative divisions.

The rose diagrams of the one-year-long wind data at the ten observational sites are shown in Fig. 2. For the seven sites (Ds2, Ds3, Ss1, Ss2, Pt1, Pt2, and Pt3) located in relatively open areas, the characteristics of the prevailing wind direction are basically manifestations of the subtropical maritime monsoon climate. In winter, the Siberian High dominates the Asian mainland, driving cold northerly winds, mainly from the north and northwest, over Zhoushan. In summer, the North Pacific Subtropical High governs the region, bringing southerly winds, predominately from the south and southeast, to the islands. The dominant wind speeds at each site are between 3.3 and 20.7 m/s. Moderate winds occur with a high probability of 76.76 % at Ds3, and strong winds are most frequent at Ss2 with a high occurrence rate of 23.86 %. A few gale winds appear at these sites with probabilities less than 0.25 %, due to the low frequency and limited duration of typhoon RUMBIA, YAGI, and AMPIL in 2018. For the three sites (Dh1, Dh2, and Ds1) that partially sheltered by nearby topography, the wind directions possess similar characteristics to the other seven sites, however, the dominant wind speeds are significantly lower. The light wind prevails the most at Dh1 with a high probability of 64.94 %, and limited strong winds are mainly recorded at Dh2 and Ds1 due to the venturi effect in mountainous regions.

3. Methods

This paper presents a three-stage methodological framework (Fig. 3) designed for wind resources assessment and offshore wind turbine site selection for multi-island areas. The framework begins with seven global wind datasets' comparative analyses through site-averaged statistical evaluations and site-specific graphical assessments to identify the most representative one for characterizing Zhoushan's local wind patterns. The optimal product serves as an accurate baseline for long-term wind energy assessment near hub height on annual, seasonal, and monthly timescales, ensuring the reliability of subsequent analyses. In the second stage, wind resources are classified by utilizing the proposed methodology, IOMCA, considering energy, risk-stability, and environment-cost factors. Finally, the framework proceeds to a multi-layer GIS-based spatial planning approach to identify unconstrained zones based on the resource classification map and then quantifies the technical potential in these areas.

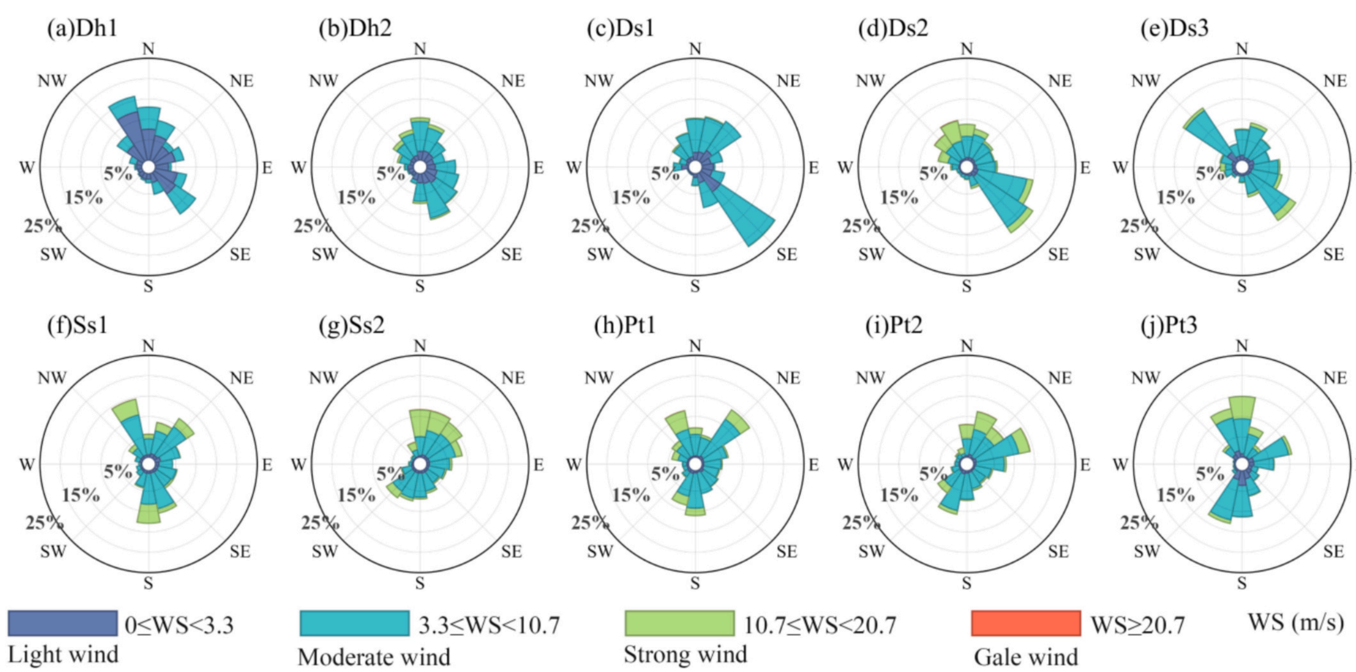

Fig. 2. Wind roses of measured wind speeds (WS) and directions at the ten observation sites. The wind speeds are categorized into 4 classes [58]: Light wind (0 m/s $\leq$ WS $<$ 3.3 m/s), Moderate wind (3.3 m/s $\leq$ WS $<$10.7 m/s), Strong wind (10.7 m/s $\leq$ WS $<$ 20.7 m/s), and Gale wind (WS $\geq$ 20.7 m/s). There are five intervals from 0 to 25 %, each representing a 5 % increase in wind speed occurrence. Note: WS is only used in the figure for brevity, while "wind speed" is used in the text.

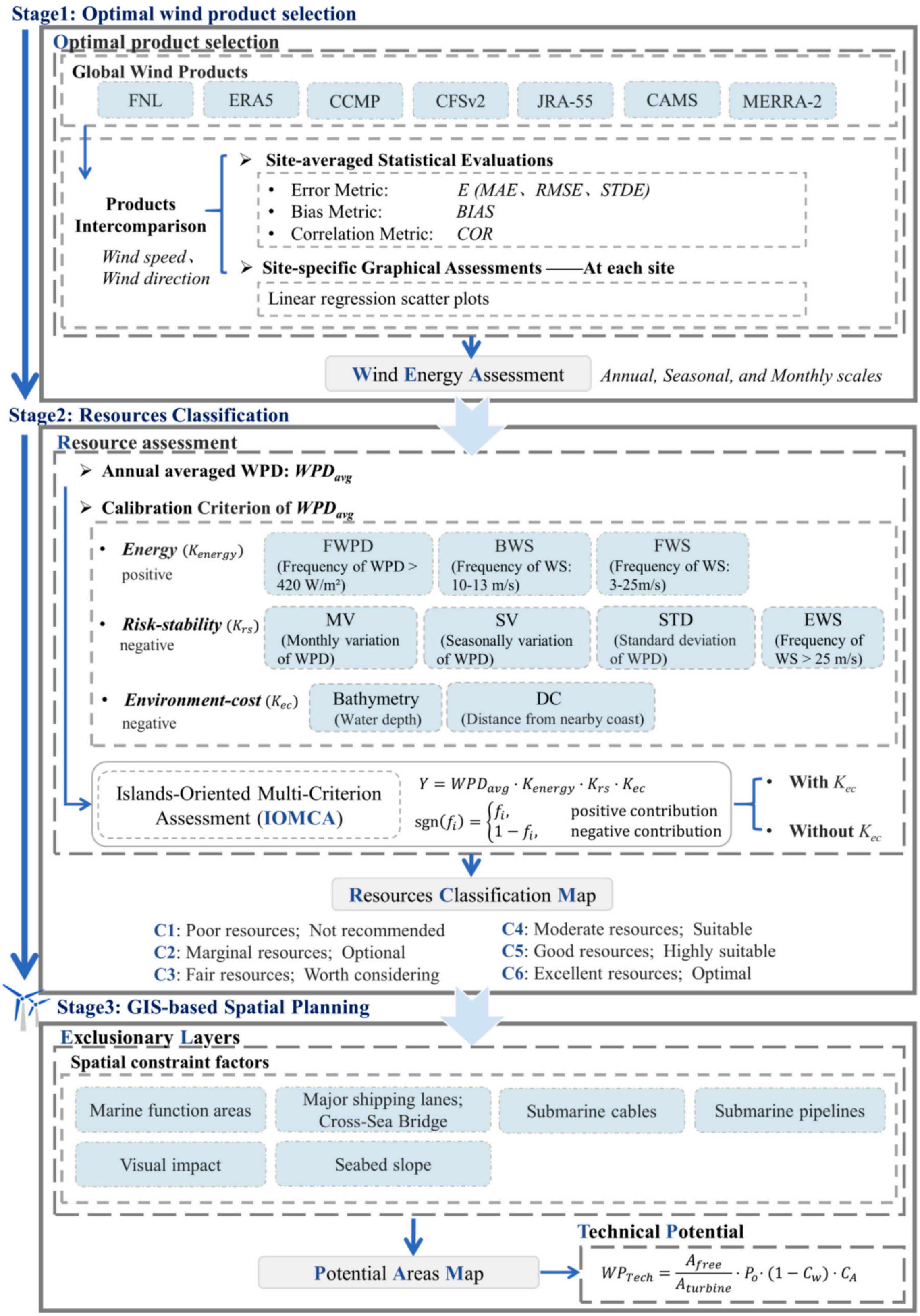

Fig. 3. Methodological framework. Abbreviations in figure: WS (wind speed); K_{energy} (energy coefficient); K_{rs} (risk-stability coefficient); K_{ec} (environment-cost coefficient); f_i (influential factors for resource classification); WP_{Tech} (technical potential); A_{free} (feasible areas free of spatial utilization); $A_{trubine}$ (average areas occupied by per turbine); P_o (annual wind energy output of a single turbine); C_w (loss rate of wake effect); C_A (turbine availability coefficient).

3.1. Wind energy assessment over Zhoushan

Seven global wind datasets, including one analysis (FNL), one multi-platform synthetic (CCMP), and five reanalysis products (ERA5, CFSv2, MERRA-2, JRA-55, and CAMS), were selected to be the candidates of the optimal one for the study area. Table 1 summarizes their contributor, temporal coverage, assimilation method, position of vertical levels, as well as temporal and spatial resolutions. Wind components u (eastward) and v (northward) at 10 m height were extracted with timestamps from each dataset to compute wind speed (m/s) and wind direction (°) in commensurate with the measurements. To ensure the consistency and comparability across given products with respective temporal resolutions, the time series of wind speed and direction were resampled to 6-hourly intervals (00:00, 06:00, 12:00, and 18:00 UTC each day), which corresponds to the coarsest temporal resolution among the selected products. A total of 1460 data points were yielded for comparison with the corresponding records of the observed data in 2018. In reference to spatial locations of the ten observational sites, the nearest neighbor interpolation was applied across the coverage domain of each dataset to determine proper grid points from which the time series associated with each site were constructed for performance evaluation.

Three metrics are considered in the study to quantify errors between the measurements (y_i) and the products (x_i) indexed by i. The comprehensive absolute error (E) is calculated as the averages of mean absolute error (MAE), root mean square error (RMSE), and standard deviation error (STDE) in the forms of

$$MAE = \frac{1}{N}\sum_{i=1}^{N}|y_i - x_i| \tag{1}$$

$$RMSE = \sqrt{\frac{1}{N}\sum_{i=1}^{N}(y_i - x_i)^2} \tag{2}$$

$$STDE = \sqrt{RMSE^2 - BIAS^2} \tag{3}$$

for each time series of wind speed and direction with N elements. The bias (BIAS), written as

$$BIAS = \frac{1}{N}\sum_{i=1}^{N}(y_i - x_i) \tag{4}$$

is utilized as the second metric to evaluate systematic deviations of the wind products relative to the observations. The linear correlation coefficient (COR) is also considered as the third metric in the following form to assess the similarity between two time series in terms of strength and pattern

$$COR = \frac{\sum_{i=1}^{N}(y_i - \bar{y})(x_i - \bar{x})}{\sqrt{\sum_{i=1}^{N}(y_i - \bar{y})^2}\sqrt{\sum_{i=1}^{N}(x_i - \bar{x})^2}} \tag{5}$$

where $\bar{y}$ and $\bar{x}$ denote the averages of the measured and the observed time series respectively. The evaluation metrics E, BIAS, and COR, provide a comprehensive assessment of each product's performance in accurately hindcasting both wind speed and wind direction over Zhoushan Archipelago. An additional set of linear regression scatter plots for wind speed at each observation site is also incorporated as a statistical visualization to provide an intuitive representation of the product's accuracy at various spatial locations. Both the site-averaged error analysis and site-specific graphical validation are considered in the evaluation to ensure the selected product is the best representation of the Zhoushan wind field.

Wind energy assessment at near-hub height is then conducted through an analysis of the spatial distribution of WPD. The WPD over an indexed period of time ($i = 1, \ldots, N$) is associated with the corresponding wind speed v_i (m/s) in the form

$$WPD = \frac{1}{2N}\sum_{I=1}^{N}\rho {v_i}^3 \tag{6}$$

where the air density at 100 m height, basically equivalent to the near-hub-height [60,61], is approximated as 1.2133 kg/m^3. If the near-hub-height wind speed is not available in the optimal wind product, the logarithmic wind profile is taken to extrapolate the data. The 45-year wind speed data spanning from Jan 1st, 1980 to Dec 31st, 2024 UTC provides a sufficiently long record to capture interannual and decadal variability, ensuring a statistically robust basis for estimating the distribution of WPD. The hourly wind speed data is also linearly interpolated into a dense mesh (2000 × 800) with a spatial resolution of 0.55 km to allow better resource classification in the next stage. The annual, seasonal, and monthly WPD is then derived from the optimal wind dataset and evaluated according to the wind energy categories shown in Table 2.

3.2. Resource classification

Wind energy assessment in the first stage provides the evaluation of WPD at near-hub-height across the study area. The following resource classification in the second stage (Fig. 3) formalizes the quantitative analysis into standard categories to indicate project feasibility and guide deployment strategies. The weighted-additive multi-criteria decision-making methods are widely adopted in wind resource classification, particularly for its capability to systematically integrate wind data with socio-environmental criteria [48,49]. Weighted criteria, such as wind speed, grid proximity, environmental impact, and others, are linearly aggregated to yield a total score by which optimal zones for wind farms are identified. When implemented in area with multiple islands, however, these methods are not efficient in accentuating regional differences, leading to featureless classifications. The OHI is another composite index used to identify high-quality wind energy development areas [55,62]. It emphasizes regions with high and stable resource by

Table 2
Classes of wind energy at 100 m height Refs. [59].

WPD Class	WPD (W/m^2)	WPD Class	WPD (W/m^2)
1 (Poor)	0–200	5 (Abundant)	560–670
2 (Limited)	200–260	6 (Exceptional)	670–820
3 (Fair)	260–420	7 (Substantial)	820–1060
4 (Sufficient)	420–560	8 (Exceptional)	> 1060

Table 1
Specifies of the selected wind products.

Datasets type	Dataset	Institution	Temporal coverage	Assimilation system	Vertical level (m)	Temporal res. (h)	Spatial res.
Analysis	FNL	NCEP	1999-present	3D-VAR	10, 20, 30, 50, 80, 100	6	1.000° lat/lon
	ERA5	ECMWF	1940-present	4D-VAR	10, 100	1	0.250° lat/lon
	CFSv2	NCEP	2011-present	3D-VAR	10	6	0.205° lat/lon
Reanalysis	JRA-55	JMA	1958–2024	4D-VAR	10	6	1.250° lat/lon
	MERRA-2	NASA	1980-present	3D-VAR	2, 10, 50	1	0.500° lat/0.625° lon
	CAMS	ECMWF	2003-present	4D-VAR	10	3	0.750° lat/lon
Multi-platform synthetic	CCMP	ECMWF	1987-present	VAM	10	6	0.250° lat/lon

multiplying WPD with the frequency of WPD exceeding a threshold value and meanwhile penalizes areas with high seasonal variation by dividing the monthly variation of WPD, ultimately prioritizing optimal hotspots for wind farm development. Nevertheless, the difficulty of proper weight-balance between these factors and the shortage of other influencing factors limit the use of OHI in Zhoushan Archipelago.

To efficiently highlight the inter-regional resource differences and properly balance multiple influential factors in multi-island areas, we propose a new wind resource classification scheme, IOMCA. Altogether nine normalized factors (f_1-f_9) were considered in the study, and the details are listed in Table 3 with respect to their categories and contributions. Three of them, including FWPD, FWS, and BWS are directly associated with wind energy potential; four others, composed of EWS, MV, SV, and STD, are considered as risk-stability factors; while the remaining two, Bathymetry and DC, belong to the environmental-cost category. From the contribution point of view, three of the nine factors, including FWPD, FWS, and BWS, are positively correlated to the wind energy. Regions exhibiting elevated values of these factors demonstrate enhanced wind energy availability and favorable turbine operational conditions, and particularly, areas with high BWS values indicate increased frequency of optimal winds (10–12 m/s) for peak turbine efficiency. The rest six factors, on the contrary, exhibit negative correlations. Among the six factors, a high frequency of extreme wind speeds (EWS) poses risks to turbine integrity and safety. Elevated standard deviation (STD) of the annual WPD (A_i, $i = 1, \ldots, N$) relative to the averaged WPD value μ over N years indicates large absolute temporal fluctuations, which may lead to greater variations in power output. Large seasonal variation (SV) and monthly variation (MV) of WPD signify greater relative temporal fluctuations at shorter timescales, thereby potentially degrading the power output stability. Both of the environmental-cost factors exert constraints on offshore wind energy development, as deeper waters and greater distances from the coast significantly increase technical and economic challenges for turbine deployment. All nine factors are min-max normalized to be re-scaled into the range of $f_i \in [0,1]$ before classification computation.

At each grid point across the study domain, a normalized expectation score (Y), ranging from the least favorable value 0 to the optimal value 1, is determined through the following form

$$Y = WPD_{avg} \cdot K_{energy} \cdot K_{rs} \cdot K_{ec} \tag{7}$$

$$K_{energy} = \sum_{i=1}^{3} \mathrm{sgn}(f_i); K_{rs} = \sum_{i=4}^{7} \mathrm{sgn}(f_i); K_{ec} = \sum_{i=8}^{9} \mathrm{sgn}(f_i) \tag{8}$$

$$\mathrm{sgn}(f_i) = \begin{cases} f_i, & \text{positive contribution} \\ 1 - f_i, & \text{negative contribution} \end{cases} \tag{9}$$

where the WPD_{avg} represents the annual averaged WPD, the coefficients K_{energy}, K_{rs}, *and* K_{ec} denote the calibration from the energy-related factors, risk-stability-related factors, and the environmental-cost-related factors, respectively. Each adjustment coefficient K is defined as the sum of the corresponding $\mathrm{sgn}(f_i)$ indexed by $i = 1, \ldots, N$, where $\mathrm{sgn}(f_i)$ is a monotonically increasing function assigning f_i to positive contributors or its complement ($1-f_i$) to negative contributors. The resources classification map, derived from the Y-scores across the domain, is comprised of six categorization areas as defined in Table 4: Class 1 signifies poor expected wind resources and is not recommended for wind turbine installation; Class 2 represents marginal wind resources where wind turbine installation is optional; Class 3 denotes fair wind resources, making them worthy of consideration; Class 4 corresponds to moderate wind resources suitable for turbine installation; Class 5 identifies good wind resources that are highly suitable for development; Class 6 highlights optimal sites with excellent wind resource potential. All unconstrained areas, except for Class 1, are available for offshore wind turbine installation, with higher class levels indicating greater preference.

3.3. GIS-based spatial planning

In the third stage (Fig. 3), areas free of spatial constraints for offshore wind energy development are identified, and their technical potential is subsequently assessed. Initially, GIS techniques are applied to exclude all prohibited areas from the resource classification map generated in the previous stage, thereby delineating the unconstrained areas suitable for wind energy deployment. Table 5 specifies six categories of spatial constraint factors, along with their corresponding prohibited area and data sources. The spatial constraints are defined as follows: (a) policy-designated marine function areas, including port and shipping areas, tourism, leisure, and entertainment areas, ocean protection areas, and special utilization areas [63]; (b) 1 km buffer zones around the major shipping lanes and the Cross-Sea Bridge [64]; (c) 500 m buffer zones around submarine cables and pipelines [64]; (d) areas with seabed slopes exceeding 10° [66]; and (e) visual impact areas, defined as 10 km buffer zones from populated coasts to minimize conflicts with coastal activities [51]. The populated coasts are identified based on population density data at a 100 m grid resolution (per hectare) derived from [67], where valid values indicate populated areas, while NoData regions are interpreted as low-population-density zones and thus considered less visually sensitive. Regarding seabed sediments, since the study area is predominantly composed of mixed fine-grained sediments, such as sand, silt, and clay [68], which are generally suitable for the construction of offshore wind turbines [64,69], the distribution is not further visualized in this study.

Subsequently, the technical potential WP_{Tech} (TWh/yr), defined as the average annual energy output of all installable wind turbines within the unconstrained areas $\left(A_{free}/A_{turbine}\right) \cdot P_o$, after accounting for losses $(1 - C_W) \cdot C_A$, is quantified to inform practical implementation strategies. The wind farm layout in our analysis consists of an 8-row by 15-column configuration of each unit, with turbines spaced 8D apart and a 20 km buffer zone maintained between adjacent units, to minimize wake and

Table 3
Influential factors for wind resource classification.

Vari-able	Factor	Category (K)	Description	Contri-bution
f_1	FWPD	Energy at 100 m height	Frequency of appliable WPD exceeds 420 W/m^2	Positive
f_2	FWS		Frequency of appliable wind speeds between 3 and 25 m/s	
f_3	BWS		Frequency of favorable wind speeds between 10 and 13 m/s	
f_4	EWS	Risk-stability at 100 m height	Frequency of extreme wind speeds exceeding 25 m/s	Negative
f_5	MV		Monthly variation of WPD: $(WPD_{mmax} - WPD_{mmin})/WPD_{avg}$ ①	
f_6	SV		Seasonally variation of WPD: $(WPD_{smax} - WPD_{smin})/WPD_{avg}$ ②	
f_7	STD		Standard deviation of WPD: $\sqrt{\frac{1}{N}\sum_{i=1}^{N} \lvert A_i - WPD_{avg} \rvert^2}$ ③	
f_8	Bath-ymetry	Environmental-cost	Water depth	
f_9	DC		Distance from the nearby coasts	

① The WPD_{mmax} and WPD_{mmin} denote the maximum and the minimum monthly WPD, and the WPD_{avg} is the annual averaged WPD.
② The WPD_{smax} and WPD_{smin} denote the maximum and the minimum seasonally WPD.
③ The A_i represents WPD at specific year indexed by $i = 1, \ldots, N$.

Table 5
Spatial constraint factors and corresponding prohibited area for offshore wind turbines installation.

Factor	Prohibited area	Data Source
Marine function areas a. Port and shipping areas b. Tourism, leisure, and entertainment areas c. Ocean protection areas d. Special utilization areas	Within designated boundaries [63]	Data from National Marine Functional Zoning (2011−2020) published by Zhejiang Provincial Development and Reform Commission [65]
Major shipping lanes; Cross-Sea Bridge	1 km buffer [64]	Public data on Zenodo (*doi:* https://doi.org/10.5281/zenodo.6361694)
Submarine cables	0.5 km buffer [64]	Submarine Cable Map (*https://www.submarinecablemap.com*)
Submarine pipelines	0.5 km buffer [64]	Global Oil and Gas Data-Web Map (*http://worldmap.harvard.edu/data/geonode:natural_gas_pipelines_j96*)
Seabed slope	Slope > 10° [66]	General Bathymetric Chart of the Ocean (*https://www.gebco.net/*)
Visual impact	10 km buffer around populated coasts [51]	WorldPop 2020 dataset (*https://hub.worldpop.org/*) [67]

Table 4
Classification schemes of expected wind resources for offshore wind turbine installation.

Class	Expectation scores	Expected potential resources	Suggestion for offshore wind turbine installation
1	$0.0 \le Y < 0.3$	poor	not recommended
2	$0.3 \le Y < 0.6$	marginal	optional
3	$0.6 \le Y < 0.7$	fair	worth considering
4	$0.7 \le Y < 0.8$	moderate	suitable
5	$0.8 \le Y < 0.9$	good	highly suitable
6	$0.9 \le Y \le 1.0$	excellent	optimal

turbulence effects on a turbine from its neighboring turbines in the array [17,64].

$$WP_{Tech} = \frac{A_{free}}{A_{turbine}} \cdot P_o \cdot (1 - C_w) \cdot C_A \tag{10}$$

where the A_{free} (km^2) represents the unconstrained areas; $A_{trubine}$ (km^2) denotes the averaged areas occupied by each turbine, which depends on the layout of the offshore wind farm; P_o (MWh/yr) is the average annual wind energy output of a single turbine at a specific location based on its power curve; C_w, the loss rate of wake effect, equals 8 % [64]; and the turbine availability coefficient C_A is assumed to be 95 % [70].

In this study, three offshore wind turbines from various manufacturers with distinct characteristics are selected, including GW175–8.0, Vestas V164–8.0, and Siemens SWT-6.0–154, for the technical potential calculation. Their specifications, including rated power, rotor diameter D, rated speed, cut-in speed, and cut-off speed, are listed in Table 6. The power curve of each considered wind turbine is presented in Fig. S1.

4. Results

4.1. Wind energy assessment over Zhoushan

Wind energy assessment described in the following three sub-sections serves as the foundation for the subsequent wind resource classification (Section 4.2) and GIS-based spatial planning (Section 4.3). The sub-section 4.1.1 conducts a comparative evaluation of seven global wind datasets through both site-averaged statistical evaluations and site-specific graphical assessments to identify the most representative one for characterizing Zhoushan's wind field. The long-term near-hub-height wind energy assessment is then assessed in sub-section 4.1.2 based on the optimal wind product. The sub-section 4.1.3 quantifies the temporal variability of WPD in terms of annual standard deviation, seasonal variation, and monthly variation.

4.1.1. Optimal wind product selection

Table 7 presents the site-averaged statistical analysis results, including absolute errors (MAE, RMSE, STDE, and E), correlation, and absolute bias. In terms of the absolute errors, ERA5 is revealed as the top-performing one with the lowest comprehensive errors E for both wind speeds (1.98 m/s) and wind direction (34.55°), along with the lowest errors in MAE, RMSE, and STDE for wind direction, although its STDE for wind speed marginally trails the lowest one (1.83 m/s of FNL) by only 0.01 m/s. FNL ranks the second to ERA5, exhibiting slightly higher error metrics for both wind speeds and wind direction across most indicators, including E, MAE, RMSE, and directional STDE. The remaining products, including CFSv2, CCMP, JRA-55, and MERRA-2, present substantially higher absolute errors for both wind speeds and direction, although CAMS showing comparable performance to FNL in wind speeds. In terms of the correlation, the inter-dataset differences are not significant for both wind speeds (ΔCOR <0.04) and wind direction (ΔCOR <0.05), with ERA5 showing the strongest correlation with the observed data.

Regarding the absolute bias, the wind products achieving the lowest absolute values show slight variations in wind speeds and wind direction. JRA-55 obtains the minimal score in wind speeds (1.09 m/s), and most of the remaining products show comparable accuracy within a narrow range of 1.20–1.28 m/s, including CAMS, ERA5, CCMP, CFSv2, and FNL in descending order, while MERRA-2 exhibits the maximum deviation (1.40 m/s). In terms of wind direction, CAMS achieves the lowest absolute bias (13.24°), with CFSv2, JRA-55, ERA5, CCMP, and FNL trailing behind in that order, whereas MERRA-2 again presents the

Table 6
Specifications of wind turbines.

Wind turbines	Rated power (MW)	Rotor diameter D (m)	Rated wind speed (m/s)	Cut-in wind speed (m/s)	Cut-out wind speed (m/s)
GW175–8.0 ①	8.0	175.0	12	3	25
V164–8.0 ②	8.0	164.0	13	4	25
SWT6.0–154 ④	6.0	154.0	13	4	25

① https://www.goldwind.com/cn/windpower/product-gw6s.
② https://en.wind-turbine-models.com/turbines/1419-mhi-vestas-offshore-v164-8.0-mw.
③ https://en.wind-turbine-models.com/turbines/657-siemens-swt-6.0-154.

Table 7
Statistical evaluations of annual wind speeds and direction averaged across ten sites, over Zhoushan.

	Products	Errors				Correlation	Bias
		MAE	RMSE	STDE	E	COR	BIAS
Wind speeds (m/s)	ERA5	**1.82**	**2.29**	1.84	**1.98**	**0.81**	1.21
	CFSv2	1.98	2.50	2.05	2.18	0.79	1.26
	CCMP	1.93	2.47	2.03	2.14	0.77	1.24
	JRA-55	1.93	2.45	2.06	2.15	0.78	**1.09**
	MERRA-2	2.00	2.50	1.97	2.16	0.78	1.40
	CAMS	1.85	2.33	1.89	2.02	**0.81**	1.20
	FNL	1.85	2.33	**1.83**	2.01	**0.81**	1.28
Wind direction (°)	ERA5	**27.20**	**40.13**	**36.31**	**34.55**	**0.56**	13.55
	CFSv2	28.63	42.05	38.64	36.44	**0.56**	13.33
	CCMP	29.36	42.47	38.92	36.92	0.51	13.69
	JRA-55	29.71	43.14	39.61	37.49	0.53	13.54
	MERRA-2	29.78	43.42	39.58	37.59	0.53	14.72
	CAMS	28.06	41.28	37.70	35.68	0.54	**13.24**
	FNL	27.71	40.69	36.77	35.06	0.55	13.74

Note: All metrics are presented in absolute values.

Table 8
Area and percentage of the unconstrained area across six classes. Each class is categorized into regions with water depth less than 50 m (lt 50 m) and greater than 50 m (gt 50 m).

	Class	**C1**	**C2**	**C3**	**C4**	**C5**	**C6**	**Sum**
Area (km^2)	lt 50 m	1136.59	4718.55	1171.03	1549.89	1377.68	378.86	10,332.60
	gt 50 m	861.05	3134.22	0.00	0.00	0.00	0.00	3995.27
	Sum	1997.64	7852.78	1171.03	1549.89	1377.68	378.86	14,327.87
Percentage of unconstrained area (%)	lt 50 m	7.93	32.93	8.17	10.82	9.62	2.64	72.11
	gt 50 m	6.01	21.88	0.00	0.00	0.00	0.00	27.89
	Sum	13.94	54.81	8.17	10.82	9.62	2.64	100.00

Table 9
WP_{Tech} of the unconstrained area across six classes, considering three turbine types. Each class is categorized into regions with water depth less than 50 m (lt 50 m) and greater than 50 m (gt 50 m).

Class Turbine	C1	C2	C3	C4	C5	C6	Sum (TWh/yr)
	lt / gt 50 m	lt / gt 50 m	lt / gt 50 m	lt / gt 50 m	lt / gt 50 m	lt / gt 50 m	
GW175–8.0	2.42 / 1.87	9.97 / 6.68	2.35 / 0.00	3.00 / 0.00	2.52 / 0.00	0.67 / 0.00	29.48
V164–8.0	1.99 / 1.55	8.21 / 5.51	1.92 / 0.00	2.44 / 0.00	2.02 / 0.00	0.54 / 0.00	24.18
SWT6.0–154	1.63 / 1.27	6.72 / 4.51	1.57 / 0.00	1.99 / 0.00	1.65 / 0.00	0.44 / 0.00	19.78

largest deviation (14.72°) suggesting its consistent systemic errors across both wind speeds and direction. Although JRA-55 and CAMS perform best in terms of minimizing systematic errors in wind speed and wind direction, respectively, ERA5 shows absolute biases within a comparable range. In addition, ERA5 consistently outperforms the other products across all absolute error metrics and correlation, demonstrating its overall advantage across the study area. Its higher temporal (hourly) and spatial (0.25°) resolutions, compared to JRA-55 and CAMS (as shown in Table 1), further enhance its suitability for regional wind energy assessment and finer-scale applications. Taken together, these results indicate ERA5 provides the best overall performance in site-averaged statistical evaluations of both wind speeds and direction.

The accuracy of wind products is further evaluated at specific locations through linear regression lines and scatter plots, along with embedded sub-tables presenting E, BIAS, and COR values (Fig. 4). Only the wind speed, which is proportional to the cube root of WPD and can have direct impacts on wind energy calculations, is considered in this plot; while the wind direction, primarily affecting turbine orientation and layout, is not the focus of the analysis here. Supported by the error metrics in those sub-tables, the distribution of the scatter points and fit lines of the seven products relative to the 1:1 diagonal line ($k = 1$) reveals distinct site-specific characteristics among the seven wind products. ERA5 demonstrates the most stable performance across all sites, consistently ranking within the top three for both E and bias metrics at nearly every location. It achieves maxima accuracy, with the smallest E values at Ds3 (1.54 m/s), Ss1 (1.47 m/s), and Pt3 (1.23 m/s), and maintains a top-three ranking at Ds2, Ss2, and Pt2, only slightly dropping to the fourth at Ss2. The only exceptions are the three sheltered sites, Dh1, Dh2, and Ds1, where FNL performs better. In terms of systematic bias, ERA5 performs a low bias across most stations, ranking within the top three at Ds2, Ds3, Pt2, and Pt3. Furthermore, ERA5 yields the highest correlation with observations at most sites, reflecting its robustness in capturing observed wind patterns.

In contrast, other datasets, particularly FNL, JRA-55, and CFSv2, demonstrate site-dependent characteristics, with each exhibiting optimal performance only at specific locations. For instance, FNL outperforms other products at the three sheltered sites, with fit lines closest to the diagonal and consistent lowest E and biases, while it performs the worst at other open sites, including Ds2, Ds3, Ss1, Ss2, Pt1, Pt2, and Pt3. Similarly, CFSv2 shows top accuracy at several exposed open stations (Ds2, Ss2, and Pt2), while obtaining the largest E and systematic biases at the three sheltered sites, subsequently limiting its overall reliability. JRA-55 obtains the lowest E values at Pt1 sites and exhibits the lowest biases at several open sites, while lacking consistency across the region. Despite the narrow range of correlation differences ($\Delta COR \in [0.02, 0.09]$) among all products at the ten sites, ERA5 stands out for combining high correlation, low errors, and minimal bias in general, making it the most balanced and dependable dataset at most sites across the study area. Given the comprehensive advantage of ERA5 in the site-averaged statistical evaluation and the stable performance in the site-

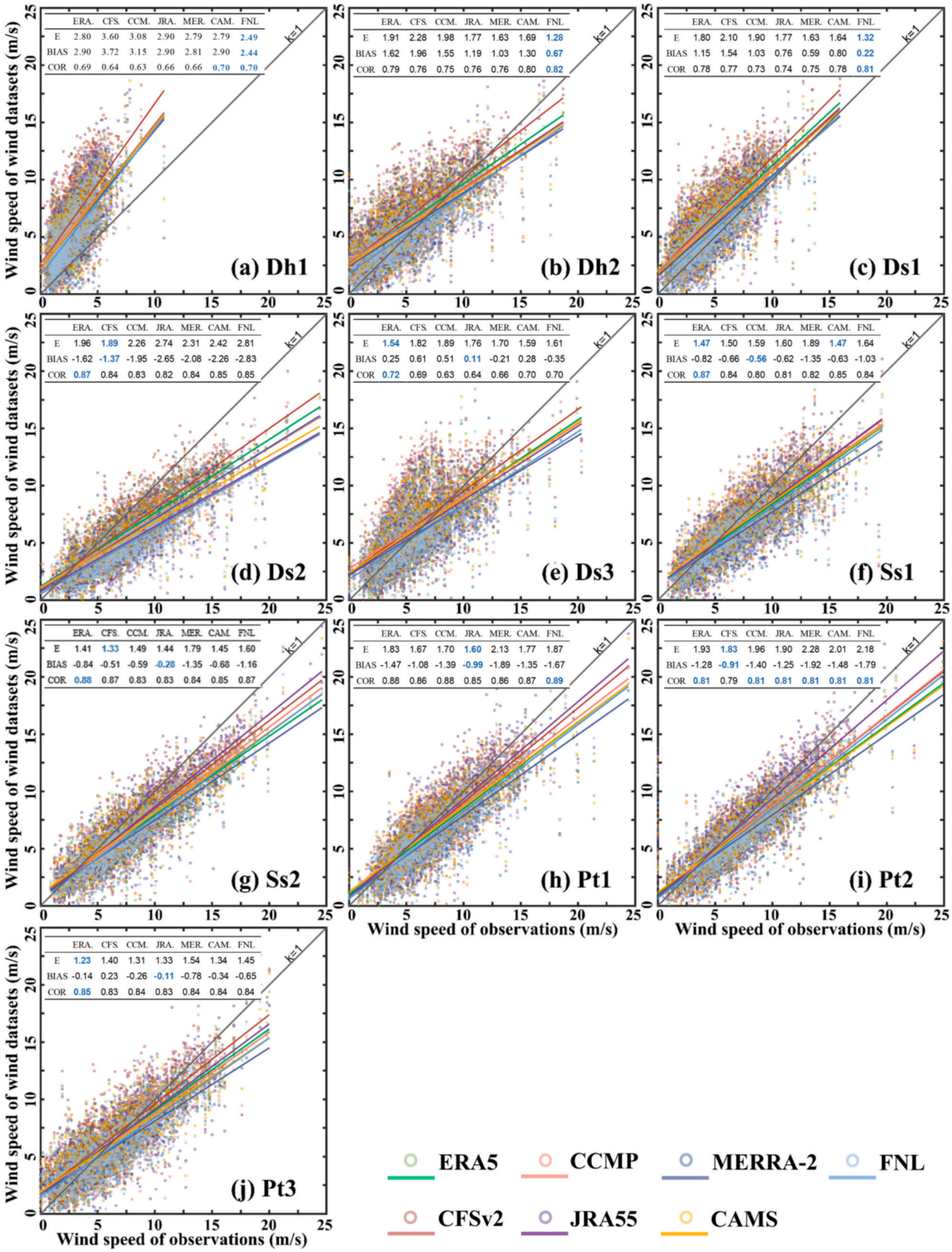

Fig. 4. Site-specific linear regression scatter plots of seven wind products' annual wind speeds according to measurements. Each subplot includes one statistic evaluation table of the corresponding site. The minimum error values in the table are highlighted in bold blue font for emphasis. (For interpretation of the references to colour in this figure legend, the reader is referred to the web version of this article.)

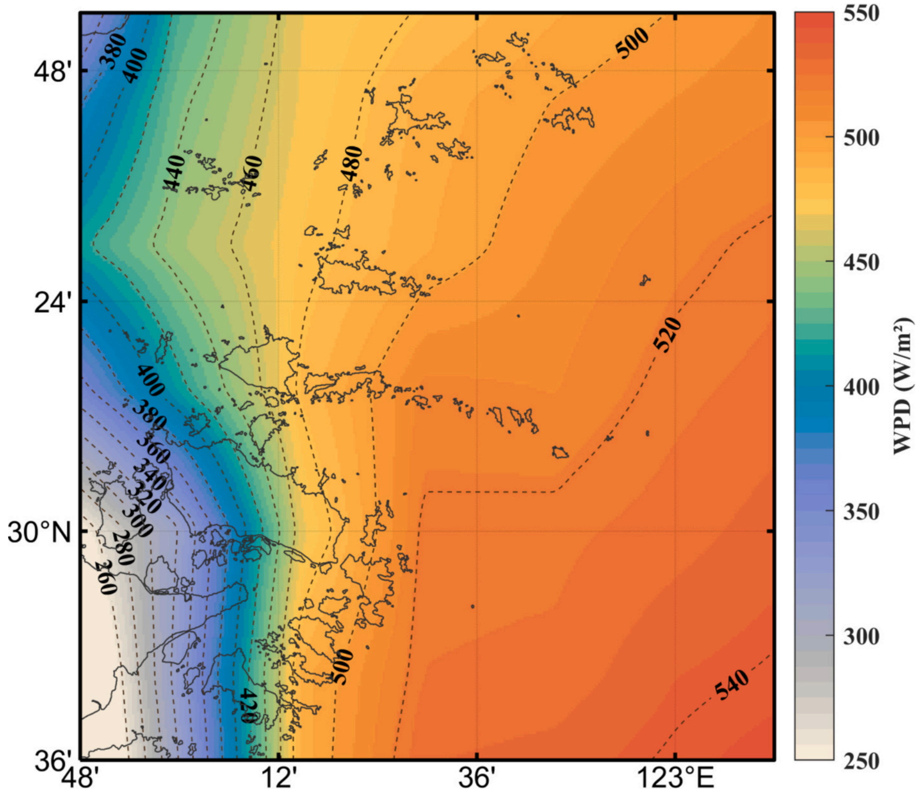

Fig. 5. Annual WPD during the 45-year period. The WPD contours at 20 W/m^2 intervals.

specific assessment, it is selected as the optimal dataset to represent Zhoushan's wind field for the subsequent wind energy assessment. One-year long observational wind field data is utilized in the study for validation purpose, which could be further improved if evenly distributed data with longer time span becomes available in the future.

4.1.2. Long-term wind energy assessment

As shown in Fig. 5, the annual WPD over the 45 years throughout Zhoushan ranges from about 260 W/m^2 to 550 W/m^2, exhibiting a general west-southeast gradient, with values increasing and contours widening from nearshore west to the offshore east. The entire study area falls within the Class 3 (fair) and Class 4 (sufficient) wind energy levels, with the 420 W/m^2 contour traversing through the western part of the area, indicating that most areas possess sufficient wind energy. High wind energy potential (> 500 W/m^2) concentrates in the southeastern open sea, encircled by SsA, DsD, DsA, and PtB islands. Moving north-westward, the WPD gradually decreases from nearly 500 W/m^2 to about 360–440 W/m^2 in Hangzhou Bay. The WPD reaches its lowest values in the southwestern nearshore island-cluster region (260–360 W/m^2), where wind energy is substantially lower than the offshore open sea, mainly due to complex terrain, surface roughness, and thermal effects [71]. More detailed assessments of seasonal and monthly wind energy characteristics are provided in the Supplementary Text of the Supplementary Material.

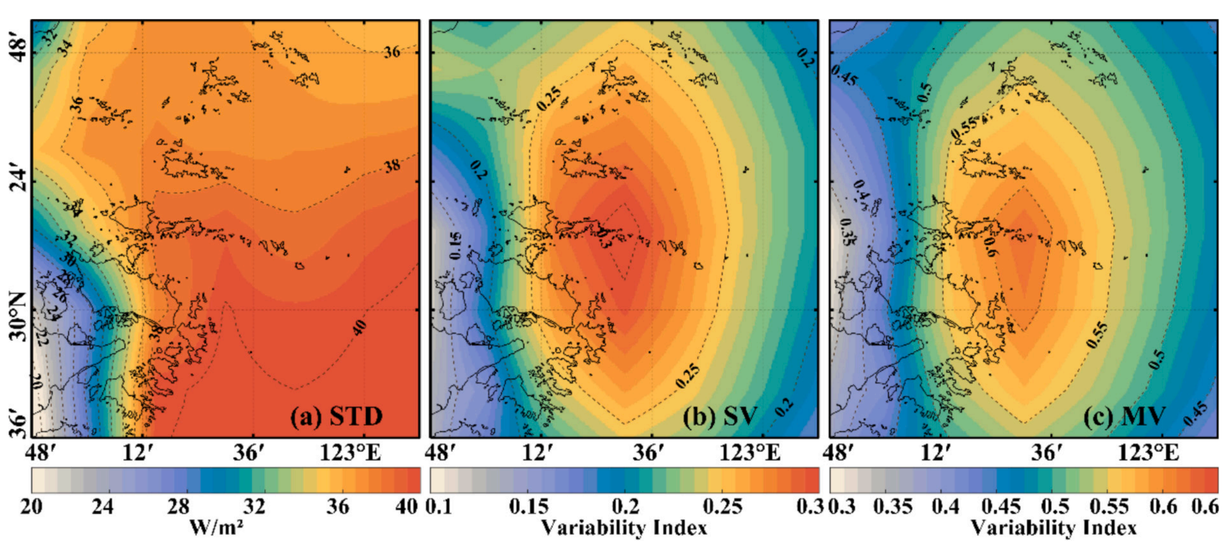

Fig. 6. Distribution of and STD (a), SV (b), and MV (c) during the 45-year period.

4.1.3. Wind energy stability and variability

Fig. 6 presents the annual standard deviation, seasonal variation, and monthly variation of WPD over 45 years in three subplots. The STD (Fig. 6a) across the study area ranges from 20 to 40 W/m^2, approximately one-tenth of the annual WPD (Fig. 5), suggesting generally consistent interannual wind energy stability with limited year-to-year fluctuations throughout the region. The spatial distribution of STD displays a northwest-southeast gradient, similar to that of the annual WPD. Higher STD (38–40 W/m^2) occurs in the southeastern offshore region, indicating the largest absolute variability in annual WPD, thereby resulting in more pronounced interannual variations in power output. The STD gradually decreases northward, from the northeastern seas

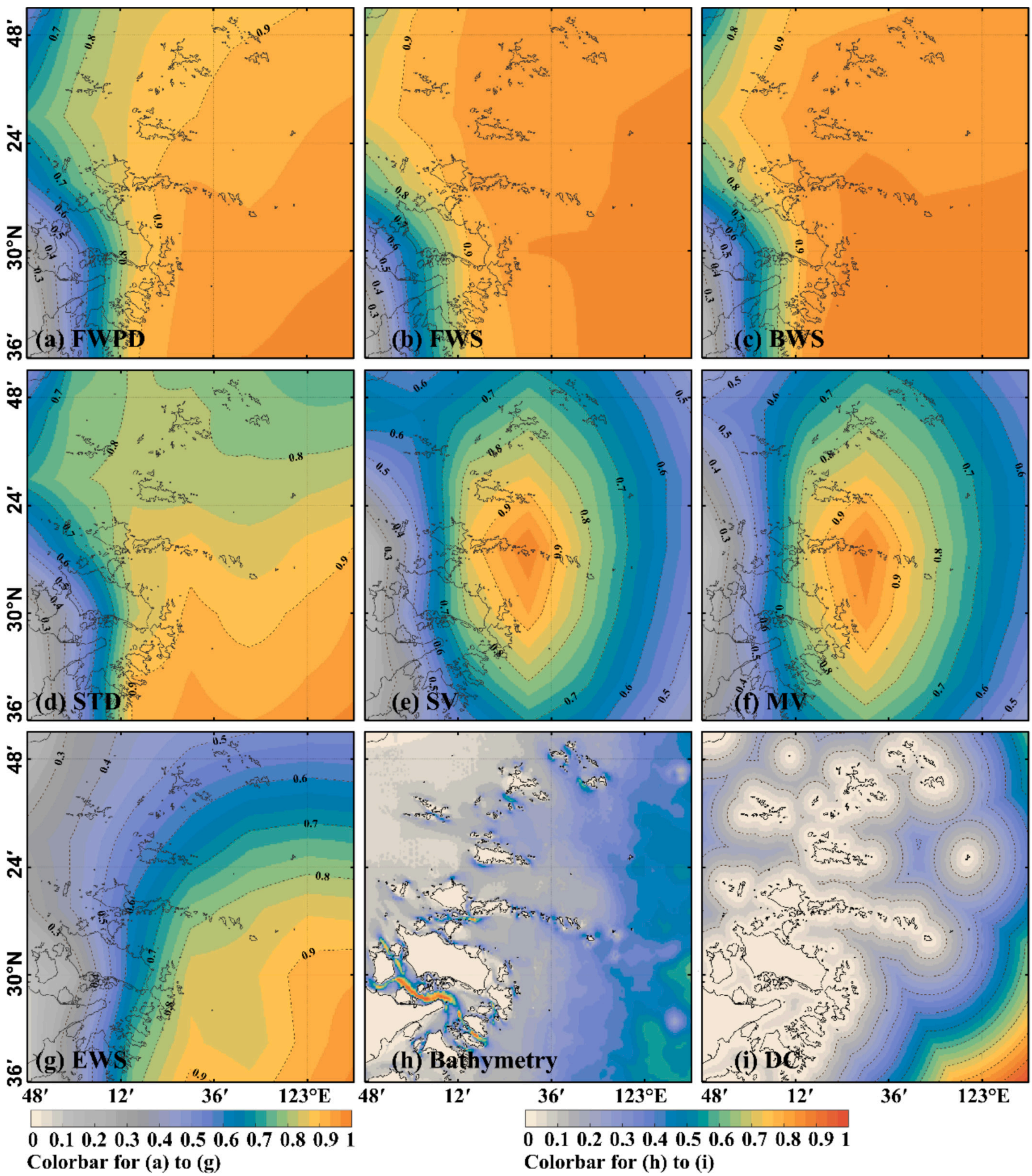

Fig. 7. Normalized influential factors. Subplots (a) to (c) correspond to energy-related factors. Subplots (d) to (g) are risk factors. Subplots (h) and (i) represent environment-related factors.

around SsA-SsB-DsD-DsB islands alignment (about 36–38 W/m^2) to Hangzhou Bay (about 30–36 W/m^2). Lower STD, ranging from 22 to 28 W/m^2, is observed in the southwestern nearshore island-cluster region, indicating negligible absolute wind energy variation and thereby relatively stable interannual power output.

The MV (Fig. 6c), ranging from 0.30 to 0.65, is approximately twice as large as the SV (0.10–0.30, Fig. 6b), indicating greater monthly WPD variability than seasonal variability over Zhoushan. This pattern is also reflected in the seasonal and monthly WPD distributions shown in Figs. S2 and S3. It suggests that the atmospheric circulation patterns are more stable at seasonal timescales, whereas monthly-scale variability is more susceptible to frequent short-term weather disturbances. Both SV and MV exhibit a concentric pattern with values peaking in the central area and gradually decreasing toward the perimeter. This variation pattern can be attributed to pronounced temporal variability in WPD values in the central region at both seasonal and monthly scales, while the remaining areas maintain more consistent WPD values throughout seasons and months. Over Zhoushan, seasonal and monthly variability peaks in the central region surrounding the PtA-DsA islands (SV: 0.30; MV: 0.65) and gradually decreasing outward, highlighting that temporal fluctuations in WPD are most pronounced in the central offshore area. The northwestern region in Hangzhou Bay exhibits relatively enhanced short-term stability with more moderate seasonal and monthly variability. The lowest variability (SV: 0.12–0.20; MV: 0.35–0.45) is observed in the southwestern nearshore island-cluster region, indicating the most temporally stable wind energy across Zhoushan.

The pronounced convexity of peak STD isopleths and spatial convergence of maximum MV/SV contours toward the central area collectively reveal that the central region between DsA and PtA islands exhibits the lowest wind energy variability across annual, seasonal, and monthly scales, over the study area. This pattern arises from localized climatic instability, driven by the central region's unique transitional position between the eastern open sea areas and the western nearshore areas, forming a dynamic natural wind-speed interface that enhances spatiotemporal variability within the local wind field. Such interface characteristics are notably detected during spring (Fig. S2a; Figs. S3c-e) and summer (Fig. S2b; Figs. S3f-h), when the strengthening oceanic monsoon gradually surpasses the weakening northwestern continental monsoon. Ha et al. have also demonstrated similar findings that land-sea contrasts and topography exert significant influence on local wind fields, particularly in coastal and complex terrain areas, where wind fields exhibit greater spatial variability [72].

4.2. Wind resources classification

4.2.1. Normalized influential factors

Having evaluated the long-term wind energy potential in the previous section, this section further assesses the wind resource distribution for wind industry development. Fig. 7 depicts the spatial distribution of the normalized energy-related factors, risk-stability-related factors, and environment-cost-related factors. In terms of the energy factors (Figs. 7a-c), a consistent southwest-northwest-southeast ascending pattern is revealed. High scores (> 0.7) are observed in most of the areas, showing favorable operational conditions for wind turbines, whereas the southwestern nearshore island-cluster area exhibits lower scores. In FWPD (Fig. 7a), excellent energy resources (scores >0.9) are detected along the eastern side of the SsA-SsB-DsD-DsA-PtB islands alignment. The scores gradually decrease northwestward, reaching 0.7–0.8 in Hangzhou Bay. In both FWS (Fig. 7b) and BWS (Fig. 7c), the majority of the open sea areas, extending eastward from the SsC-DsB-ZsA-PtC islands alignment, exhibit excellent energy resources (> 0.9). Despite a general westward decline in scores, the region east of Hangzhou Bay-ZsA-PtC islands alignment maintains higher scores with values consistently above 0.7. Areas around the alignment of PtC island and the western part of ZsA show fair resource levels, with scores between 0.6 and 0.7. The southwestern area around the west of the ZsA-PtC islands alignment experiences lower scores in FWPD, FWS, and BWS (0.3–0.6) across Zhoushan, suggesting marginal wind resource in this region.

Among the risk-stability factors (Figs. 7d-g), the normalized STD, SV, and MV (Figs. 9d-f) show that the central region between PtA and DsA islands exhibits overall the lowest wind energy stability across Zhoushan, as reflected by scores exceeding 0.8. The reduced stability may compromise the consistency of wind turbine power output, despite the excellent energy resources in these areas (Figs. 7a-c). In contrast, the southwestern nearshore regions, despite their relatively lower energy potential (Figs. 7a-c), exhibit higher energy stability, with all three scores consistently below 0.5. The remaining areas present relatively moderate wind energy stability, with scores ranging from 0.5 to 0.8. The EWS (Fig. 7g) displays a southeast-northwestern-southwestern decreasing pattern. Extending eastward from SsA-SsB-DsD-DsB-PtC islands alignment and intensifying further offshore, high-frequency extreme wind speeds occur in the southeastern open seas (scores >0.6) and poses high risks to turbine integrity and safety. The remaining areas present relatively lower frequencies (scores <0.6), indicating comparatively limited risks for turbines. Lower extreme wind speeds frequency is observed in the southwestern nearshore island-cluster region, with scores less than 0.3. Overall, the Figs. 7a-f illustrate an inverse relationship between the wind energy abundance and the corresponding stability and risk.

From an environmental-cost perspective (Figs. 7h-i), the Bathymetry and DC display complex patterns with pronounced localized variabilities because of the scattered distributions of all the islands. Water depth (Fig. 7h) increases from the western nearshore areas to eastern offshore areas in general. The deepest waters are typically found within navigation channels, particularly the one between Zhoushan Island and Ningbo City, where scores exceed 0.7. Regions characterized by deep water and significant distance from the coast are mainly located in the southeastern open seas, posing substantial technical and economic challenges for turbine installation and maintenance. In consequence, the southeastern seas are ranked as lower-priority zones for offshore wind energy development when evaluated from an environmental-cost perspective.

4.2.2. Wind resource classification map

Following the above normalized influential factors, the wind resource classification maps are developed by implementing the IOMCA method presented in Section 3.2. Fig. 8a shows the classification map considering both the energy and risk-stability factors, while Fig. 8b incorporates the environmental-cost factors to highlight their impacts on offshore areas with scattered island distributions. From the energy and risk-stability perspective (Fig. 8a), the spatial distribution exhibits a pronounced concentric pattern, which is primarily influenced by the similar pattern of SV and MV, as shown in Figs. 7e-f. In general, the Y scores decrease from 1.0 at the periphery to around 0.2 at the center. The highest scores, exceeding 0.8, are concentrated in the northeastern sea areas, closely followed by the northwestern areas in Hangzhou Bay (0.75–0.85), suggesting excellent potential resources in these regions. Areas with scores of 0.6–0.8 are primarily distributed across the southeastern offshore seas and the northern offshore seas to the north of the SsC-SsB-SsA islands alignment, indicating fair to moderate resource potential. In contrast, poor resources (scores <0.3) are concentrated in the central area around PtA and DsA islands.

When the environmental-cost factors are involved (Fig. 8b), it is notable that they play a crucial role in highlighting the distinct regional variations of wind resources in multi-island areas. The original concentric classification pattern is significantly reshaped by the DC and Bathymetry, leading to a more heterogeneous distribution with highly tortuous and fragmented boundaries. Compared to Fig. 8a, regions farther from the shore with greater water depths experience a significant decline in scores, especially in the southeastern open sea areas where scores generally fall below 0.6, corresponding to Class 1 (poor) and Class 2 (marginal) levels. On the contrary, nearshore areas with shallower

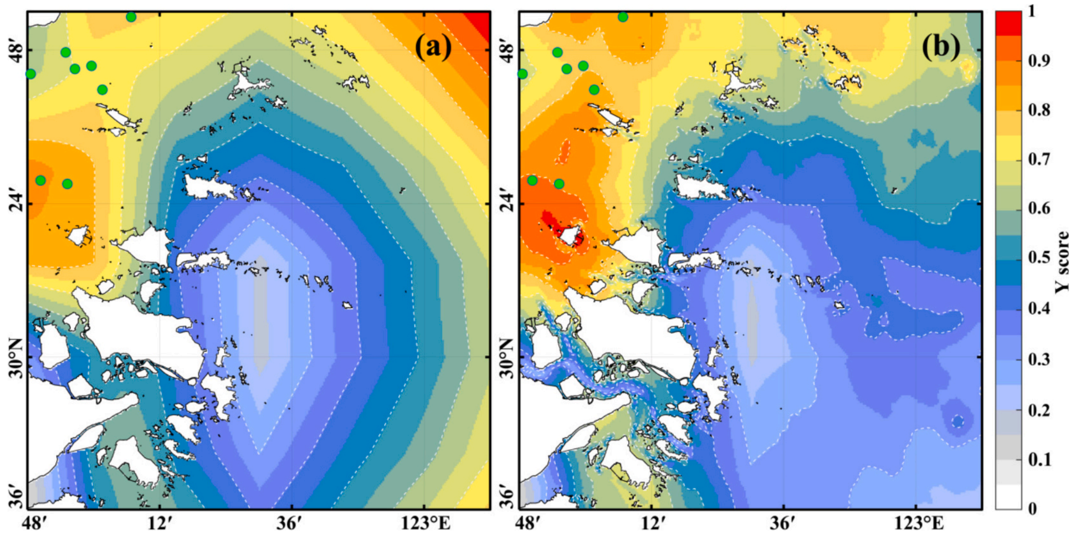

Fig. 8. Wind resource classification maps. (a) Classification considering both energy-related and risk-stability-related factors. (b) Classification considering energy-related, risk-stability-related, and environment-cost-related factors. White dotted lines denote the six classification levels. Existing offshore wind farms (interpreted from Sentinel-2 imagery, shown in Fig. S4) are marked with green points. (For interpretation of the references to colour in this figure legend, the reader is referred to the web version of this article.)

water depths exhibit a noticeable increase in Y-scores, particularly in the northern sea areas and southwestern nearshore regions, where scores exceed 0.6, indicating fair resource potential. High scores (> 0.7, Classes 4–6) are still observed in Hangzhou Bay and along the northern side of the SsA-SsB-SsC islands alignment, while the northeastern region presents a noticeable decline. The central region consistently presents overall lowest scores across the study area.

4.3. GIS-based spatial planning

Based on the wind resource classification map (Fig. 8b), unconstrained areas are developed through GIS-based spatial planning and further categorized into six classes as shown in Fig. 9. The area around DsC island that falls into the top-class C6 is identified as the optimal region for wind power development. Other highly suitable areas are concentrated in parts of Hangzhou Bay and the eastern seas of Shanghai. The third-best siting area is concentrated in the northeastern seas around SsA island, encompassing C3 (worth considering) and C4 (suitable) suitability levels simultaneously. The concentration of existing offshore wind farms, marked with orange dotted polygons, demonstrates the reliability of the results. Most of the eastern offshore seas that are classified as C2 remain a viable option depending on specific project requirements. The regions not recommended for turbine installation over Zhoushan are concentrated in the central and the southeasternmost C1 regions, owing to their low energy stability, high frequency of extreme winds, and great water depth, despite exhibiting high wind energy potential.

The technology potential of unconstrained areas is subsequently quantified to provide a reference for practical application. Note that the recommendation level for offshore turbine installation based on the classification map is independent of the estimated technical potential. Table 8 summarizes area and percentage of those unconstrained areas across the six classes, while Table 9 presents their technical potential in terms of WP_{Tech} considering three turbine types. Giving the varying construction costs and maintenance challenges of different offshore wind turbine types, the unconstrained areas are divided into two categories, depths below 50 m for fixed-bottom turbines and depths between 50 and 1000 m for floating turbines [73,74]. Construction priority in the results gives to the areas within 50-m water depth to minimize construction costs and reduce maintenance challenges. According to Table 8, a total of 14,327.87 km^2 area is identified as unconstrained in the study area, of which 10,332.60 km^2 lies in waters shallower than 50 m. Areas suitable for floating wind turbines are concentrated in C1 and C2, totaling 3995.27 km^2 and representing 27.88 % of the overall unconstrained area. The technical potential is sensitive to the specifications of wind turbines, as shown in Table 9. Among the three turbines, the GW175–8.0 performs the best across the unconstrained areas in Zhoushan, generating the highest technical potential of 29.48 TWh/yr, including 8.55 TWh/yr contributed by floating turbines, owing to its high rated power and relatively low cut-in wind speed. The V164–8.0 turbine yields a moderate technical potential of 24.18 TWh/yr. The minimum potential (19.78 TWh/yr) is produced by SWT6.0–154, which has the lowest rated power among these turbines. Within the available regions (C2-C6) for offshore wind turbine installation, the maximum technical potential is estimated at 25.19 TWh/yr based on the GW175–8.0, with 6.68 TWh/yr contributed solely by floating turbines in region C2. The technical potential in the optimal region C6 (0.67 TWh/yr) is much lower than that of the optional region C2 (16.65 TWh/yr). It is primarily because the geographic area available for wind energy development of C6 (378.86 km^2, 2.64 % of the total unconstrained area) is only 4.8 % of that in C2 (7852.78 km^2, account for 54.81 %), as shown in Table 8.

5. Discussion

In this study, a new wind resource classification scheme, IOMCA, is developed to efficiently highlight inter-regional variations of wind resource potential and properly balance multiple influential factors in multi-island areas. The performance of IOMCA is further evaluated through comparison with two other approaches. Fig. 10a presents the classification map derived from the index-based OHI method [55,62] that integrates three wind-resource factors (WPD, FWPD, and MV) by using the formula $Y = \left(WPD_{avg} \cdot FWPD\right)/MV$. The weighted-additive approach integrates multiple normalized influential factors into a single index through assigned weights and is calculated as $Y = \sum_{i=1}^{N} a_i \cdot sgn\left(f_i\right)$. In Fig. 10b, the widely used multi-criteria decision-making technique, AHP [75–77], is applied to determine the weights a_i of each influential factor $sgn(f_i)$. The weight sets, which pass the consistency test with consistency ratio below 0.1, are presented in Table S1.

As shown in Fig. 10a, the index approach produces a relatively coarse spatial pattern and therefore fails to capture fine-scale regional

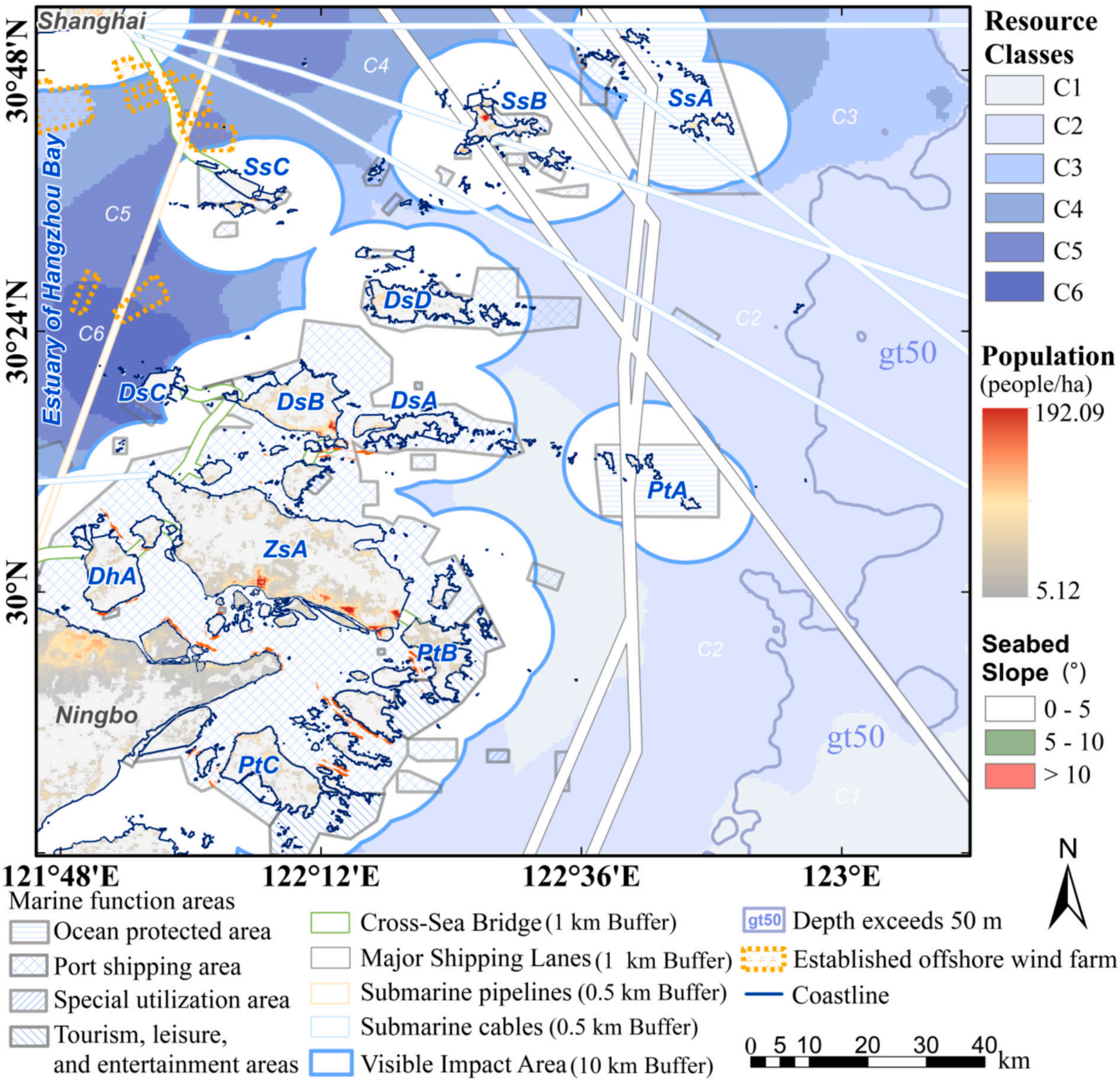

Fig. 9. Potential areas for offshore wind turbine installation. The areas are classified into six classes (C1-C6) based on the resource classification map in Fig. 10b. Spatial constraints, including marine function areas, Cross-Sea Bridge, major shipping lanes, submarine pipelines and cables, visible impact areas, and seabed slope restrictions, are overlaid to exclude unsuitable areas. Existing offshore wind farms are marked with orange dotted polygons. Areas with water depth greater than 50 m are delineated by purple boundaries labeled "gt50". (For interpretation of the references to colour in this figure legend, the reader is referred to the web version of this article.)

variations, owing to its reliance on a limited set of wind energy factors and the difficulty of proper weight-balance between unnormalized factors. Although the existing offshore wind farms (labeled by green points) fall within feasible development regions with scores between 0.3 and 0.7, these areas are not classified as the highly preferred zones by OHI. This inconsistency indicates that the method could roughly identify viable sites at a coarse resolution but lacks sufficient detail to distinguish optimal sites, thereby limiting its effectiveness for precise siting decisions in multi-island areas.

The weighted-additive method (Fig. 10b) presents general features of wind resource potential through balancing diverse or even contradictive factors. The existing wind farms are detected in regions with scores between 0.7 and 0.9, demonstrating the method's capability to broadly identify viable sites. However, as WPD, the most direct indicator of wind energy, carries a much higher weight than other factors in the scoring formulation, the final classification map is primarily influenced by this factor. Consequently, the map exhibits limited score gradients across the study area, with most regions falling into high scores (> 0.7), and the spatial characteristics of other factors are largely obscured. For example, the negative impacts of SV and MV around the central region are less pronounced in this approach, whereas they are clearly reflected by the IOMCA method (Fig. 8b). Although weight adjustment can be made according to practical considerations, the assignments remain sensitive to regional characteristics and expert judgement, which would reduce the robustness and reproducibility of the weighted-additive approach across diverse areas.

By comparison, the unweighted IOMCA method (Fig. 8b) integrates multiple factors in a way that preserves their relative importance while maintaining balanced contributions across both inter-category trade-offs and intra-category factors. Specifically, in IOMCA, WPD serves as an independent core indicator of wind energy potential, while other influential factors are applied multiplicatively as corrective terms to adjust WPD. Factors with similar importance are grouped together (e.g., DC and Depth, categorized as environment-cost factors) and treated

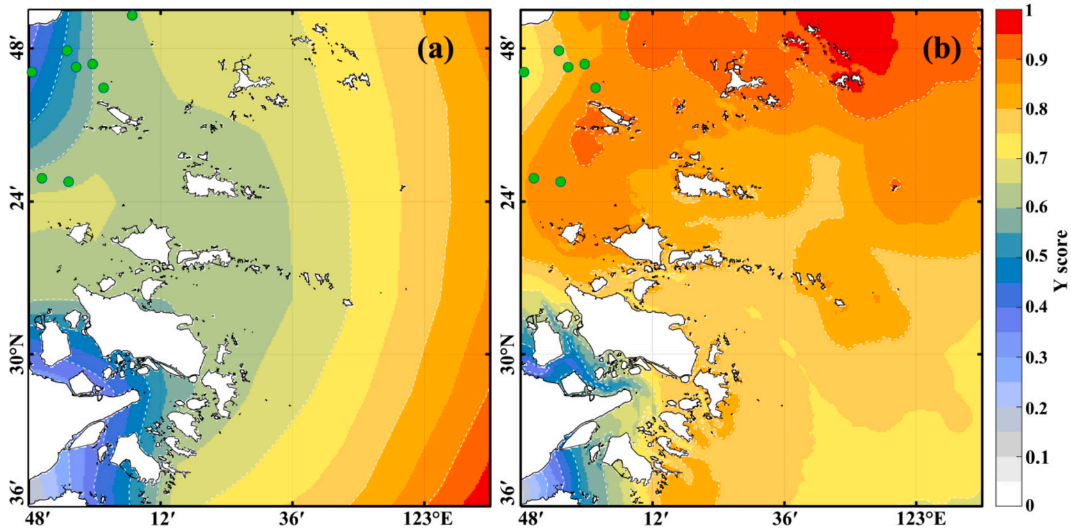

Fig. 10. Wind resource classifications derived from (a) the index approach and (b) the weighted-additive approach. Existing offshore wind farms are marked with green points. (For interpretation of the references to colour in this figure legend, the reader is referred to the web version of this article.)

equally within each group, while groups are combined multiplicatively to maintain independence and accentuate differences. This formulation design allows the method to amplify variations among different factors, enhancing the visibility of inter-regional variations. Overall, the IOMCA method offers a robust, reproducible, and refined unweighted multiplicative framework for offshore wind siting decisions in multi-island areas with complex environmental conditions, providing a new way for resource assessment.

6. Conclusions

In recent years, the rapid development of offshore wind energy has significantly heightened interests in precise wind resource assessment and advanced turbine deployment methodologies. The paper presents a three-stage methodological framework for wind energy assessment and offshore wind turbine site identification in the Zhoushan Archipelago. A long-term assessment of near-hub-height wind energy is conducted using the optimal wind dataset for characterizing local wind patterns. To capture regional variations in wind resources, energy, risk-stability, and environmental-cost factors are integrated through utilizing the IOMCA method. Based on the resulting wind resource classification map, the unconstrained offshore wind turbine zones are identified through GIS-based spatial planning, and the technical potential of each classified zone is subsequently quantified.

Over Zhoushan, the annual WPD computed from the optimal wind dataset ERA5 ranges between 260 and 550 W/m^2, with increasing trend from west to southeast. Most areas exhibit sufficient wind energy potential with WPD exceeding 420 W/m^2 (above Class 4). The annual standard deviation of WPD exhibits the same increasing gradient with values ranging from 20 to 40 W/m^2. The seasonal (SV: 0.3–0.65) and monthly (MV: 0.1–0.3) variations of WPD show a concentric pattern with values peaking in the central area around DsA and PtA islands. When three types of influential factors are all considered in the proposed classification method, areas of high wind resource potential ($>$ 0.7) are concentrated in Hangzhou Bay and along the northern side of the SsA-SsB-SsC islands alignment. Except for the central Zhoushan region and the southeasternmost region (Class 1), most of the unconstrained areas under spatial planning are available for offshore wind turbine installation, with higher classes indicating greater suitability. Areas close by the DsC island (C6) are the optimal sites for wind energy development. Other highly suitable areas (C4-C5) are concentrated in Hangzhou Bay and the eastern seas of Shanghai. The northeastern seas around SsA island, encompassing both C3 (worth considering) and C4 (suitable) levels, are ranked as the third-recommended sites. By considering three types of offshore wind turbines, the maximum technical potential reaches 29.48 TWh/yr, with 25.19 TWh/yr contributed from the available regions C2-C6, while the minimum is 19.78 TWh/yr across the unconstrained areas over Zhoushan.

The proposed IOMCA method enables the integration of multiple factors while maintaining a balanced contribution across various factors. By adopting a multiplicative framework, it effectively captures regional differences in multi-islands regions characterized by complex environmental conditions. The unweighted structure also improves its robustness and transferability to other regions. The consistency between the identified optimal zones and existing offshore wind farms confirms the method's reliability. In summary, this study provides a valuable reference for renewable energy planning not only in the Zhoushan Archipelago but also in other multi-island regions worldwide.

CRediT authorship contribution statement

Honghuan Zhi: Writing – review & editing, Writing – original draft, Visualization, Validation, Methodology, Investigation, Data curation. **Han Liu:** Visualization, Data curation. **Liqin Zhou:** Visualization, Data curation. **Yifan Zhou:** Visualization, Methodology. **Feixiang Li:** Visualization, Formal analysis. **Xiaoran Wei:** Visualization, Investigation. **Yefei Bai:** Writing – review & editing, Writing – original draft, Methodology, Investigation, Funding acquisition, Formal analysis, Conceptualization.

Declaration of competing interest

The authors declare that they have no known competing financial interests or personal relationships that could have appeared to influence the work reported in this paper.

Acknowledgments

The work was supported by National Natural Science Foundation of China 42376212 (Y. B.).

Appendix A. Supplementary data

Supplementary data to this article can be found online at https://doi.org/10.1016/j.apenergy.2025.127275.

Data availability

The authors do not have permission to share data.

References

[1] International Energy Agency (IEA). Global Energy Review: CO_2 Emissions in 2021; 2022. https://wwwieaorg/reports/global-energy-review-co2-emissions-in-2021-2.
[2] United Nations Environment Programme. Emissions gap report 2022: The closing window—Climate crisis calls for rapid transformation of societies; 2022. https://wwwuneporg/emissions-gap-report-2022.
[3] Global Wind Energy Council (GWEC). Global offshore wind report 2019; 2019. https://gwecnet/global-wind-report-2019/.
[4] Rehman S, Menesy AS, Zayed ME, Zaery M, Shaikhi A, Mohandes M, et al. Synergistic sizing and energy management strategy of combined offshore wind with solar floating PV system for green hydrogen and electricity co-production using multi-objective dung beetle optimization. RINENG 2025;25:104399. https://doi.org/10.1016/j.rineng.2025.104399.
[5] Hernández CV, González JS, Fernández-Blanco R. New method to assess the long-term role of wind energy generation in reduction of CO2 emissions–case study of the European union. J Clean Prod 2019;207:1099–111. https://doi.org/10.1016/j.jclepro.2018.09.249.
[6] Mudhafar MAH, Zayed ME, Rehman S. Offshore wind-to-green hydrogen: a comprehensive review on current challenges, techno-economic analyses, environmental implications, and potential risks. Process Saf Environ 2025;107631. https://doi.org/10.1016/j.psep.2025.107631.
[7] Global wind energy council (GWEC). Global wind report 2025; 2025. https://www.gwec.net/reports/globalwindreport/2025/.
[8] Global wind energy council (GWEC). Global wind report 2024; 2024. https://www.gwec.net/reports/globalwindreport/2023/.
[9] Global wind energy council (GWEC). Global wind report 2023; 2023. https://www.gwec.net/reports/globalwindreport/2023/.
[10] Department of Energy Statistics, National Bureau of Statistics. China energy statistical yearbook; 2017. China Statistics Press Beijing, China. https://www.stats.gov.cn/zs/tjwh/tjkw/tjzl/202302/t20230215_1907891.html.
[11] Yang Y, Liu Z, Chen H, Wang Y, Yuan G. Evaluating regional eco-green cooperative development based on a heterogeneous multi-criteria decision-making model: example of the Yangtze River Delta region. Sustainability-basel 2020;12:3029. https://doi.org/10.3390/su12073029.
[12] Development and Reform Commission of Zhejiang Province. "14th Five-Year Plan" for Renewable Energy Development in Zhejiang Province; 2021. https://www govcn/xinwen/2021–03/13/content_5592681htm.
[13] Nie B, Li J. Technical potential assessment of offshore wind energy over shallow continent shelf along China coast. Renew Energy 2018;128:391–9. https://doi.org/10.1016/j.renene.2018.05.081.
[14] Sempreviva AM, Barthelmie RJ, Pryor S. Review of methodologies for offshore wind resource assessment in European seas. Surv Geophy 2008;29:471–97. https://doi.org/10.1007/s10712-008-9050-2.
[15] Carvalho D, Rocha A, Gómez-Gesteira M, Santos CS. WRF wind simulation and wind energy production estimates forced by different reanalyses: comparison with observed data for Portugal. Appl Energy 2014;117:116–26. https://doi.org/10.1016/j.apenergy.2013.12.001.
[16] Skamarock WC, Klemp JB, Dudhia J, Gill DO, Barker DM, Duda MG, et al. A description ofthe advanced research WRF version 3; 2008.475:10.5065. doi: https://doi.org/10.5065/D68S4MVH.
[17] Baldauf M, Seifert A, Förstner J, Majewski D, Raschendorfer M, Reinhardt T. Operational convective-scale numerical weather prediction with the COSMO model: description and sensitivities. Mon Weather Rev 2011;139:3887–905. https://doi.org/10.1175/MWR-D-10-05013.1.
[18] Pielke RA, Cotton W, Rea Walko, Tremback C, Lyons WA, Grasso L, et al. A comprehensive meteorological modeling system—RAMS. Meteorol Atmos Phys 1992;49:69–91.
[19] Castorrini A, Gentile S, Geraldi E, Bonfiglioli A. Increasing spatial resolution of wind resourceprediction using NWP and RANS simulation. J Wind Eng Ind Aerod 2021;210:104499. https://doi.org/10.1016/j.jweia.2020.104499.
[20] Fernández-González S, Martín ML, García-Ortega E, Merino A, Lorenzana J, Sánchez JL, et al. Sensitivity analysis of the WRF model: wind-resource assessment for complex terrain. J Appl Meteorol Clim 2018;57:733–53. https://doi.org/10.1175/JAMC-D-17-0121.1.
[21] Whiteman CD, Zhong S. Downslope flows on a low-angle slope and their interactions with valley inversions. Part I: Observations. J Appl Meteorol Clim 2008;47:2023–38. https://doi.org/10.1175/2007JAMC1669.1.
[22] Demolli H, Dokuz AS, Ecemis A, Gokcek M. Wind power forecasting based on daily wind speed data using machine learning algorithms. Energy Convers Manag 2019; 198:111823. https://doi.org/10.1016/j.enconman.2019.111823.
[23] Rasp S, Pritchard MS, Gentine P. Deep learning to represent subgrid processes in climate models. Proc Nat Acad Sci 2018;115(39):9684–9.
[24] Schultz MG, Betancourt C, Gong B, Kleinert F, Langguth M, Leufen LH, et al. Can deep learning beat numerical weather prediction? Philosophical Transactions of the Royal Society A 2021;379(2194):20200097. https://doi.org/10.1098/rsta.2020.0097.
[25] Haupt SE, Chapman W, Adams SV, Kirkwood C, Hosking JS, Robinson NH, et al. Towards implementing artificial intelligence post-processing in weather and climate: proposed actions from the Oxford 2019 workshop. Phil Trans R Soc A 2021;379(2194):20200091. https://doi.org/10.1098/rsta.2020.0091.
[26] Buckley MP, Horstmann J, Savelyev I, Carpenter JR. Direct observations of airflow separation over ocean surface waves. Nat Commun 2025;16:5526. https://doi.org/10.1038/s41467-025-61133-1.
[27] Ćorak M, Mikulić A, Katalinić M, Parunov J. Uncertainties of wave data collected from different sources in the Adriatic Sea and consequences on the design of marine structures. Ocean Eng 2022;266:112738. https://doi.org/10.1016/j.oceaneng.2022.112738.
[28] Hauser D, Abdalla S, Ardhuin F, Bidlot JR, Bourassa M, Cotton D, et al. Satellite remote sensing of surface winds, waves, and currents: where are we now? Surv Geophys 2023;44(5):1357–446. https://doi.org/10.1007/s10712-023-09771-2.
[29] Satyanarayana Gubbala C, Dodla VBR, Desamsetti S. Assessment of wind energy potential over India using high-resolution global reanalysis data. J Earth Syst Sci 2021;130:1–19. https://doi.org/10.1007/s12040-021-01557-7.
[30] Nezhad MM, Neshat M, Groppi D, Marzialetti P, Heydari A, Sylaios G, et al. A primary offshore wind farm site assessment using reanalysis data: a case study for Samothraki island. Renew Energy 2021;172:667–79. https://doi.org/10.1016/j.renene.2021.03.045.
[31] Wang Y-H, Walter RK, White C, Farr H, Ruttenberg BI. Assessment of surface wind datasets for estimating offshore wind energy along the Central California coast. Renew Energy 2019;133:343–53. https://doi.org/10.1016/j.renene.2018.10.008.
[32] Mattar C, Guzmán-Ibarra MC. A techno-economic assessment of offshore wind energy in Chile. Energy 2017;133:191–205. https://doi.org/10.1016/j.energy.2017.05.099.
[33] Kubik M, Brayshaw DJ, Coker PJ, Barlow JF. Exploring the role of reanalysis data in simulating regional wind generation variability over Northern Ireland. Renew Energy 2013;57:558–61. https://doi.org/10.1016/j.renene.2013.02.012.
[34] Agarwal A, Venugopal V, Harrison GP. The assessment of extreme wave analysis methods applied to potential marine energy sites using numerical model data. Renew Sustain Energy Rev 2013;27:244–57. https://doi.org/10.1016/j.rser.2013.06.049.
[35] Kim H-G, Kim J-Y, Kang Y-H. Comparative evaluation of the third-generation reanalysis data for wind resource assessment of the southwestern offshore in South Korea. Atmosphere-basel 2018;9:73. https://doi.org/10.3390/atmos9020073.
[36] Carvalho D, Rocha A, Gómez-Gesteira M, Alvarez I, Santos CS. Comparison between CCMP, QuikSCAT and buoy winds along the Iberian Peninsula coast. Remote Sens Environ 2013;137:173–83. https://doi.org/10.1016/j.rse.2013.06.005.
[37] Alvarez I, Gomez-Gesteira M, deCastro M, Carvalho D. Comparison of different wind productsand buoy wind data with seasonality and interannual climate variability in the southern Bay of Biscay (2000–2009). Deep-sea Res Pt Ii 2014;106:38–48. https://doi.org/10.1016/j.dsr2.2013.09.028.
[38] Carvalho D. An assessment of NASA`S GMAO MERRA-2 reanalysis surface winds. JClimate 2019;32:8261–81. https://doi.org/10.1175/JCLI-D-19-0199.1.
[39] Miao H, Dong D, Huang G, Hu K, Tian Q, Gong Y. Evaluation of northern hemisphere surface wind speed and wind power density in multiple reanalysis datasets. Energy 2020;200:117382. https://doi.org/10.1016/j.energy.2020.117382.
[40] Wang G, Wang X, Wang H, Hou M, Li Y, Fan W, et al. Evaluation on monthly sea surface wind speed of four reanalysis data sets over the China seas after 1988. Acta Oceanol Sin 2020;39:83–90. https://doi.org/10.1007/s13131-019-1525-0.
[41] Carvalho D, Rocha A, Gómez-Gesteira M, Santos CS. Comparison of reanalyzed, analyzed, satellite-retrieved and NWP modelled winds with buoy data along the Iberian Peninsula coast. Remote Sens Environ 2014;152:480–92. https://doi.org/10.1016/j.rse.2014.07.017.
[42] Ebita A, Kobayashi S, Ota Y, Moriya M, Kumabe R, Onogi K, et al. The Japanese 55-year reanalysis "JRA-55": an interim report. Sola 2011;7:149–52. https://doi.org/10.2151/sola.2011-038.
[43] Minola L, Zhang F, Azorin-Molina C, Pirooz AS, Flay R, Hersbach H, et al. Near-surface mean and gust wind speeds in ERA5 across Sweden: towards an improved gust parametrization. Clim Dynamic 2020;55:887–907. https://doi.org/10.1007/s00382-020-05302-6.
[44] Soares PM, Lima DC, Nogueira M. Global offshore wind energy resources using the new ERA-5 reanalysis. Environ Res Lett 2020;15:1040a2. https://doi.org/10.1088/1748-9326/abb10d.
[45] Carreno-Madinabeitia S, Ibarra-Berastegi G, Sáenz J, Ulazia A. Long-term changes in offshore wind power density and wind turbine capacity factor in the Iberian Peninsula (1900–2010). Energy 2021;226:120364. https://doi.org/10.1016/j.energy.2021.120364.
[46] Ruiz SAG, Barriga JEC, Martínez JA. Wind power assessment in the Caribbean region of Colombia, using ten-minute wind observations and ERA5 data. Renew Energy 2021;172:158–76. https://doi.org/10.1016/j.renene.2021.03.033.
[47] Chadee XT, Clarke RM. Large-scale wind energy potential of the Caribbean region using near-surface reanalysis data. Renew Sustain Energy Rev 2014;30:45–58. https://doi.org/10.1016/j.rser.2013.09.018.
[48] Zheng C-w, Xiao Z-n, Peng Y-h, Li C-y, Du Z-b. Rezoning global offshore wind energy resources. Renew Energy 2018;129:1–11. https://doi.org/10.1016/j.renene.2018.05.090.
[49] Zheng C-w, Li C-y, Xu J-j. Micro-scale classification of offshore wind energy resource——a case study of the New Zealand. J Clean Prod 2019;226:133–41. https://doi.org/10.1016/j.jclepro.2019.04.082.
[50] Dalkey N, Helmer O. An experimental application of the Delphi method to the use of experts. Manage Sci 1963;9(3):458–67. https://doi.org/10.1287/mnsc.9.3.458.
[51] Abramic A, Mendoza AG, Haroun R. Introducing offshore wind energy in the sea space: Canary Islands case study developed under maritime spatial planning

principles. Renew Sustain Energy Rev 2021;145:111119. https://doi.org/10.1016/j.rser.2021.111119.
[52] Demirel T, Demirel N Ç, Kahraman C. Fuzzy analytic hierarchy process and its application//fuzzy multi-criteria decision making: Theory and applications with recent developments. Boston, MA: Springer US, 2008:53–83.
[53] Tahir ZuR, Abdullah M, Ahmad S, Kanwal A, Farhan M, Saeed UB, et al. An approach to assess offshore wind power potential using bathymetry and near-hub-height reanalysis data. Ocean Eng2023;280:114458.
[54] Bahaj AS, Mahdy M, Alghamdi AS, Richards DJ. New approach to determine theImportance index for developing offshore wind energy potential sites: supported by UK and Arabian peninsula case studies. Renew Energy 2020;152:441–57.
[55] Patel RP, Nagababu G, Kachhwaha SS, Surisetty VAK. A revised offshore wind resource assessment and site selection along the Indian coast using ERA5 near-hub-height wind products. Ocean Eng 2022;254:111341. https://doi.org/10.1016/j.oceaneng.2022.111341.
[56] Zhoushan Municipal Bureau of Statistics. Zhoushan Statistical Yearbook; 2023. Zhoushan Municipal Statistics Bureau. http://zstjzhoushangovcn/col/col1229774343/indexhtml.
[57] Tennekes H. The logarithmic wind profile. Atmos Sci 1973;30(2):234–8. https://doi.org/10.1175/1520-0469(1973)030<0234:TLWP>2.0.CO;2.
[58] Huler S. Defining the wind: The Beaufort scale and how a 19th-century admiral turned science into poetry. Crown; 2007.
[59] Oh K-Y, Kim J-Y, Lee J-K, Ryu M-S, Lee J-S. An assessment of wind energy potential at thedemonstration offshore wind farm in Korea. Energy 2012;46:555–63. https://doi.org/10.1016/j.energy.2012.07.056.
[60] Gualtieri G. Improving investigation of wind turbine optimal site matching through the self-organizing maps. Energy Convers Manag 2017;143:295–311. https://doi.org/10.1016/j.enconman.2017.04.017.
[61] Pryor S, Letson F, Barthelmie R. Variability in wind energy generation across the contiguous United States. J Appl Meteorol Clim 2020;59:2021–39. https://doi.org/10.1175/JAMC-D-20-0162.1.
[62] Kamranzad B, Etemad-Shahidi A, Chegini V. Developing an optimum hotspot identifier for wave energy extracting in the northern Persian gulf. Renew Energy 2017;114:59–71. https://doi.org/10.1016/j.renene.2017.03.026.
[63] Vasileiou M, Loukogeorgaki E, Vagiona DG. GIS-based multi-criteria decision analysis for site selection of hybrid offshore wind and wave energy systems in Greece. Renew Sustain Energy Rev 2017;73:745–57. https://doi.org/10.1016/j.rser.2017.01.161.
[64] Hong L, Möller B. Offshore wind energy potential in China: under technical, spatial and economic constraints. Energy 2011;36:4482–91. https://doi.org/10.1016/j.energy.2011.03.071.
[65] Zhejiang Province Ocean and Fisheries Bureau. Zhejiang Marine Functional Zoning (2011–2020); 2018. Zhejiang Provincial Development and Reform Commission. https://zrzyt.zj.gov.cn/art/2018/10/15/art_1229098242_2344880.html.
[66] Xu LY, Yuan ZH, Peng XB, Chen WY, Cai F, Zhou YG, et al. Seismic response analysis of offshore wind turbines supported by monopiles on gently sloping sandy seabed. Ocean Eng 2025;323:120599. https://doi.org/10.1016/j.oceaneng.2025.120599.
[67] Tatem AJ. WorldPop, open data for spatial demography. Sci Data 2017;4:1–4. https://doi.org/10.1038/sdata.2017.4.
[68] Liu J, Zhu R, Li G. Rock magnetic properties of the fine-grained sediment on the outer shelf of the East China Sea: implication for provenance. Mar Geol 2003;193 (3–4):195–206. https://doi.org/10.1016/S0025-3227(02)00660-6.
[69] Kim Y, Lim JS, Kim HJ, Choi S. A comprehensive review of foundation designs for fixed offshore wind turbines. Int J Nav Arch Ocean 2025;17:100643. https://doi.org/10.1016/j.ijnaoe.2025.100643.
[70] Stehly T, Duffy P, Mulas Hernando D. Cost of Wind Energy Review: 2024 Edition [R]. National Renewable Energy Laboratory (NREL), Golden, CO (United States), 2024.
[71] Djath B, Schulz-Stellenfleth J, Cañadillas B. Study of coastal effects relevant for offshore wind energy using spaceborne synthetic aperture radar (SAR). Remote Sens 2022;14(7):1688. https://doi.org/10.3390/rs14071688.
[72] Ha K-J, Shin S-H, Mahrt L. Spatial variation of the regional wind field with land–sea contrasts and complex topography. J Appl Meteorol Clim 2009;48:1929–39. https://doi.org/10.1175/2009JAMC2105.1.
[73] Wu X, Hu Y, Li Y, Yang J, Duan L, Wang T, et al. Foundations of offshore wind turbines: Areview. Renew Sustain Energy Rev 2019;104:379–93. https://doi.org/10.1016/j.rser.2019.01.012.
[74] Gualtieri G. Analysing the uncertainties of reanalysis data used for wind resource assessment: a critical review. Renew Sustain Energy Rev 2022;167:112741. https://doi.org/10.1016/j.rser.2022.11274.
[75] Saaty TL. The analytic hierarchy process: Planning, priority setting, resource allocation. New York, NY: Mcgraw-Hill; 1980.
[76] Jangid J, Bera AK, Joseph M, Singh V, Singh T, Pradhan B, et al. Potential zones identification for harvesting wind energy resources in desert region of India–a multi criteria evaluation approach using remote sensing and GIS. Renew Sustain Energy Rev 2016;65:1–10. https://doi.org/10.1016/j.rser.2016.06.078.
[77] Pelser T, Weinand JM, Kuckertz P, Mckenna R, Lissen J, Stolten D, et al. Reviewing accuracy & reproducibility of large-scale wind resource assessments. Adv Appl Energy 2024;13:100158. https://doi.org/10.1016/j.adapen.2023.100158.